AGU PUBLICATIONS

JGR

Journal of Geophysical Research: Solid Earth

RESEARCH ARTICLE

10.1002/2014JB011686

Key Points:
- First core-log-seismic correlation in the central South China Sea basin
- The fossil ridge and subbasin boundary acted as major sedimentary barriers
- Seismic facies and migration of depocenter responded to tectonic events

Correspondence to:
C.-F. Li,
cfl@tongji.edu.cn

Citation:
Li, C.-F., et al. (2015), Seismic stratigraphy of the central South China Sea basin and implications for neotectonics, *J. Geophys. Res. Solid Earth*, *120*, 1377–1399, doi:10.1002/2014JB011686.

Received 12 OCT 2014
Accepted 3 FEB 2015
Accepted article online 7 FEB 2015
Published online 16 MAR 2015

Seismic stratigraphy of the central South China Sea basin and implications for neotectonics

Chun-Feng Li[1], Jiabiao Li[2], Weiwei Ding[2], Dieter Franke[3], Yongjian Yao[4], Hesheng Shi[5], Xiong Pang[5], Ying Cao[1], Jian Lin[6], Denise K. Kulhanek[7], Trevor Williams[8], Rui Bao[9], Anne Briais[10], Elizabeth A. Brown[11], Yifeng Chen[12], Peter D. Clift[13], Frederick S. Colwell[14], Kelsie A. Dadd[15], Iván Hernández-Almeida[16], Xiao-Long Huang[17], Sangmin Hyun[18], Tao Jiang[19], Anthony A. P. Koppers[14], Qianyu Li[1], Chuanlian Liu[1], Qingsong Liu[20], Zhifei Liu[1], Renata H. Nagai[21], Alyssa Peleo-Alampay[22], Xin Su[23], Zhen Sun[24], Maria Luisa G. Tejada[25], Hai Son Trinh[26], Yi-Ching Yeh[27], Chuanlun Zhang[1], Fan Zhang[6], Guo-Liang Zhang[28], and Xixi Zhao[1]

[1]State Key Laboratory of Marine Geology, Tongji University, Shanghai, China, [2]Key Laboratory of Submarine Geoscience, Second Institute of Oceanography, State Oceanic Administration, Hangzhou, China, [3]Federal Institute for Geosciences and Natural Resources, Hannover, Germany, [4]Guangzhou Marine Geological Survey, Guangzhou, China, [5]China National Offshore Oil Company Ltd. Shenzhen Branch, Shenzhen, China, [6]Woods Hole Oceanographic Institution, Woods Hole, Massachusetts, USA, [7]International Ocean Discovery Program, Texas A&M University, College Station, Texas, USA, [8]Lamont-Doherty Earth Observatory, Columbia University, Palisades, New York, USA, [9]Geologcal Institute, Swiss Federal Institute of Technology, Zürich, Switzerland, [10]Géosciences Environnement Toulouse, Centre National de la Recherche Scientifique, University of Toulouse, Toulouse, France, [11]College of Marine Science, University of South Florida, St. Petersburg, Florida, USA, [12]Key Laboratory of Marginal Sea Geology, Guangzhou Institute of Geochemistry, Chinese Academy of Sciences, Guangzhou, China, [13]Department of Geology and Geophysics, Louisiana State University and A. & M. College, Baton Rouge, Louisiana, USA, [14]College of Earth, Ocean and Atmospheric Sciences, Oregon State University, Corvallis, Oregon, USA, [15]Department of Earth and Planetary Sciences, Macquarie University, North Ryde, New South Wales, Australia, [16]Institute of Geography/Oeschger Centre for Climate Change Research, University of Bern, Bern, Switzerland, [17]State Key Laboratory of Isotope Geochemistry, Guangzhou Institute of Geochemistry, Chinese Academy of Sciences, Guangzhou, China, [18]Marine Environment and Conservation Research Division, Korea Institute of Ocean Science and Technology, Ansan, South Korea, [19]Department of Marine Science and Engineering, Faculty of Earth Resources, China University of Geosciences, Wuhan, China, [20]State Key Laboratory of Lithospheric Evolution, Institute of Geology and Geophysics, CAS, Beijing, China, [21]Department of Physical, Chemical and Geological Oceanography, Universidade de São Paulo, São Paulo, Brazil, [22]National Institute of Geological Sciences, University of the Philippines, Quezon City, Philippines, [23]School of Marine Geosciences, China University of Geosciences, Beijing, China, [24]South China Sea Institute of Oceanology, CAS, Guangzhou, China, [25]Japan Agency for Marine-Earth Science and Technology, Yokosuka, Japan, [26]Department of Science and Technology, Ministry of Natural Resources and Environment, Hanoi, Vietnam, [27]Taiwan Ocean Research Institute, Kaohsiung City, Taiwan, [28]Key Laboratory of Marine Geology and Environment, Institute of Oceanology, Chinese Academy of Sciences, Qingdao, China

Abstract Coring/logging data and physical property measurements from International Ocean Discovery Program Expedition 349 are integrated with, and correlated to, reflection seismic data to map seismic sequence boundaries and facies of the central basin and neighboring regions of the South China Sea. First-order sequence boundaries are interpreted, which are Oligocene/Miocene, middle Miocene/late Miocene, Miocene/Pliocene, and Pliocene/Pleistocene boundaries. A characteristic early Pleistocene strong reflector is also identified, which marks the top of extensive carbonate-rich deposition in the southern East and Southwest Subbasins. The fossil spreading ridge and the boundary between the East and Southwest Subbasins acted as major sedimentary barriers, across which seismic facies changes sharply and cannot be easily correlated. The sharp seismic facies change along the Miocene-Pliocene boundary indicates that a dramatic regional tectonostratigraphic event occurred at about 5 Ma, coeval with the onsets of uplift of Taiwan and accelerated subsidence and transgression in the northern margin. The depocenter or the area of the highest sedimentation rate switched from the northern East Subbasin during the Miocene to the Southwest Subbasin and the area close to the fossil ridge in the southern East Subbasin in the Pleistocene. The most active faulting and vertical uplifting now occur in the southern East Subbasin, caused most likely by the active and fastest subduction/obduction in the southern segment of the Manila Trench and the collision between the northeast Palawan and the Luzon arc. Timing of magmatic intrusions and seamounts constrained by seismic stratigraphy in the central basin varies and does not show temporal pulsing in their activities.

1. Introduction

The central South China Sea (SCS) basin is floored primarily by oceanic crust. Figure 1 shows the central basin, which is confined by the continent-ocean boundary (COB) and is comprised of three major subbasins, namely, the East, Southwest, and Northwest Subbasins. Dating of seismic sequence boundaries and studies of seismic facies in the central basin are critical to understanding regional tectonostratigraphic evolution, but these efforts have been hampered previously for two main reasons. The first is that basement highs often developed near the COB [e.g., *Li et al*., 2010, 2013], which prevent direct and continuous stratigraphic correlation between the central basin and rift basins in the continental slope, where stratigraphic boundaries can be determined from commercial wells. The strike of these basement highs is often parallel to the continental margin. These structures resulted mostly from either differential continental extension and rifting or uplifting linked to the onset of seafloor spreading [*Li et al*., 2013; *Expedition 349 Scientists*, 2014]. The second is the lack of stratigraphic well constraints in the central basin. However, these problems are being alleviated. Recently, very dense coverage of reflection seismic lines became available around the COB, and five new sites were drilled in the central basin during the International Ocean Discovery Program (IODP) Expedition 349 [*Expedition 349 Scientists*, 2014], providing an unprecedented opportunity for studying seismic stratigraphy and the opening history of the SCS and how sedimentary records responded to regional tectonic events.

Structurally and bathymetrically, the SCS basin is complicated with extinct spreading centers, transform faults, ridges, and late-stage seamount volcanism after the cessation of seafloor spreading [e.g., *Yan et al*., 2006; *Xu et al*., 2012] (Figure 1). These structures likely affected sediment transport and ocean circulation, but we previously had no way to quantify these effects. While their presence can often make stratigraphic correlation more difficult, careful interpretation of seismic horizons and facies can help better decipher the timing of tectonic activities of these structures.

Extensive discussions and close collaborations were developed among several research institutions and oil companies during the early preparation of the scientific proposal leading to IODP Expedition 349 [*Li et al*., 2013]. This led to a collection of multichannel reflection seismic (MCS) data from different resources (Table 1), making it possible to examine seismic sequences and facies of the entire central basin based on key seismic profiles and their correlation with logging/coring data at the IODP Expedition 349 sites and Ocean Drilling Program (ODP) Leg 184 sites [*Wang et al*., 2000] (Figure 1).

We build a regional stratigraphic framework by focusing on major geological boundaries (Table 2), which are well constrained by shipboard biostratigraphic and lithostratigraphic analyses [*Expedition 349 Scientists*, 2014]. With carefully selected seismic profiles, stratigraphic correlation is possible even between the continent-ocean transition zone and the central basin, circumventing basement highs that often exist near the continent-ocean boundary and prevent direct correlation. Abrupt changes in seismic facies across boundaries of subbasins are observed both temporally and spatially. Seismic facies between sequence boundaries are often characteristic and distinctive, allowing relatively straightforward regional correlation, particularly within subbasins. The calibrated seismic sequence boundaries also allow us to estimate the timing of postspreading volcanism, faulting and vertical movement in the central basin.

2. Regional Tectonic Framework

Before the Early Cretaceous, the southeast Eurasian area was strongly deformed by the subduction of the Paleo-Pacific plate, forming a massive plateau and subsequent continental arc volcanisms [e.g., *Zhou and Li*, 2000; *Li and Li*, 2007; *Shi and Li*, 2012]. At around 100 Ma, the subduction either ceased or retreated eastward [*Zhou et al*., 2006], and the entire region entered a new phase of pervasive continental margin rifting, which continued into the early Cenozoic and ultimately facilitated the opening of the SCS (Figure 1) [*Shi and Li*, 2012]. The seafloor spreading ages of the SCS basin was disputed until recently [*Taylor and Hayes*, 1980, 1983; *Briais et al*., 1993; *Yao et al*., 1994; *Hsu et al*., 2004; *Li and Song*, 2012; *Barckhausen et al*., 2014], but IODP Expedition 349 and recent deep tow magnetic surveys have helped unravel the details of the basin history [*Expedition 349 Scientists*, 2014; *C.-F. Li et al.,* 2014; *Koppers and Expedition 349 Scientists*, 2014]. The East Subbasin started opening at ~33 Ma and stopped around 15 Ma, and the seafloor spreading in the Southwest Subbasin initiated at ~23.6 Ma and terminated at about 16 Ma [*C.-F. Li et al.,* 2014].

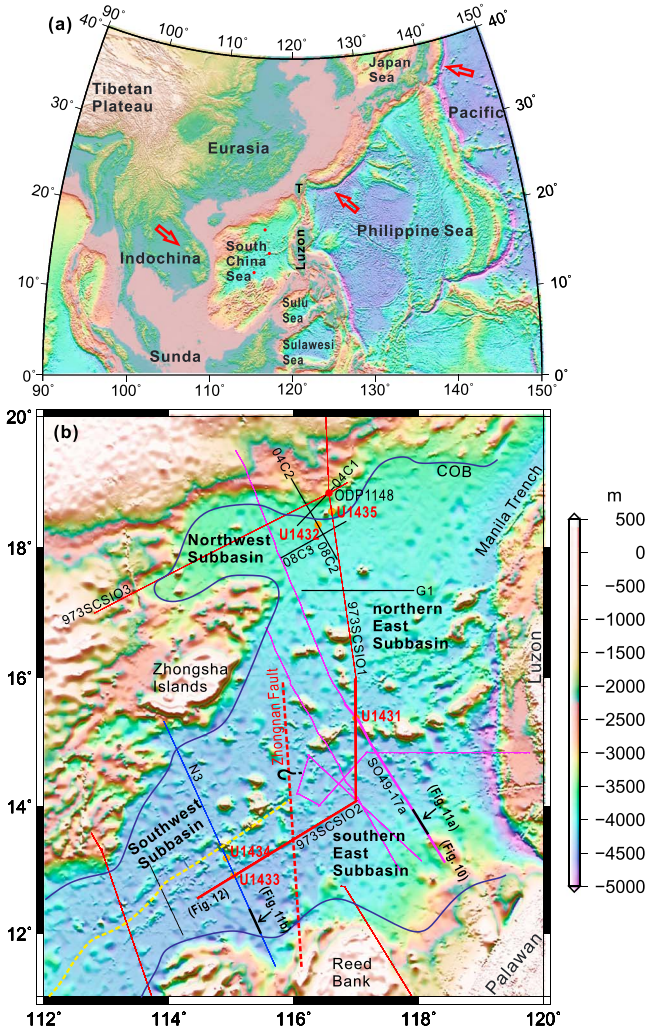

Figure 1. (a) Regional tectonic framework. T = Taiwan Island. The red arrows show the directions of plate movement. The red dots are sites drilled during IODP Expedition 349. (b) Bathymetry map of the South China Sea. Seismic lines presented in this study are labeled. The yellow dashed line indicates the relict spreading center in the Southwest Subbasin. The seamount chain in the East Subbasin divides it into the northern East Subbasin and southern East Subbasin. The orange circles are sites drilled during IODP Expedition 349 and red circle during ODP Leg 184. The thin red, black, blue, and purple lines are seismic lines. Segments of these seismic lines shown in later figures are highlighted in bold lines. COB = continent-ocean boundary.

The Luzon Arc is believed to be formed within the Philippine Sea plate with the eastward subduction of the SCS lithosphere (or westward obduction of the Philippine Sea plate) (Figure 1). It is assumed that the subduction started soon after the cessation of seafloor spreading in the SCS at about 15 Ma [*Briais et al.*, 1993; *Yang et al.*, 1996]. The initial subduction probably developed along one of the preexisting transform faults, which should have been widespread in the western Pacific. The Taiwan orogeny (Figure 1), among the most active and the youngest orogens in the world, started to build up several million years ago [*Biq*, 1972; *Chai*, 1972; *Teng*, 1990], due to the continued westward movement of the Luzon Arc and its oblique collision with the Eurasian continental margin. Likewise, the approaching Luzon also collided with the Palawan continental block in the southern margin of the SCS [e.g., *Hall*, 2002; *Liu et al.*, 2014], and this process continues today.

The Cenozoic magmatism in the region can be divided into three stages, Paleocene-Eocene (prespreading), Oligocene-middle Miocene (synspreading), and late Miocene-Quaternary (postspreading) [*Yan et al.*, 2006]. The prespreading magmatism predominantly occurred on the northern margin of the SCS and in South China coastal areas and shows a bimodal affinity [*Xu et al.*, 2012]. This bimodal magmatism may have resulted from double-layered convection in a magma chamber under an extensional setting associated with lithosphere thinning [*Chung et al.*, 1994, 1997]. The second-stage synspreading magmatism occurred along fissures or fault intersections within extensionally faulted depressions. Volcanism contemporaneous with seafloor spreading in the SCS was very weak in the margins and adjacent areas [*Yan et al.*, 2006]. Postspreading magmatism is strong along the lower slope of the northern margin of the SCS and in the central basin [*Lüdmann and Wong*, 1999; *Lüdmann et al.*, 2001; *Yan et al.*, 2001]. They can be easily identified from geophysical data and high-resolution bathymetric map [*Wang et al.*, 2014]. Most known major seamounts in the central SCS basin (Figure 1) are believed to be emplaced after the seafloor spreading stopped at about 15 Ma. K-Ar and ^{40}Ar-^{39}Ar ages of dredged samples from seamounts as well as volcanoclastic records are all younger than 15 Ma [*Wang et al.*, 1985; *Kudrass et al.*, 1986; *Yan et al.*, 2008; *Han*, 2011; *Expedition 349 Scientists*, 2014], the estimated cessation age of seafloor spreading in the SCS. Most of these seamounts are along, or to the north of, the relict spreading center (Figure 1) and are composed mainly of alkali basalts with subordinate tholeiites that display oceanic island basalt-type geochemical characteristics [*Xu et al.*, 2012].

Table 1. Summary of Seismic Data Used in This Study and ODP/IODP Drill Sites That They Cross

MCS Line Name	ODP/IODP Sites	Acquisition Date	Channels
08C2	U1432	2008	480
08C3	U1432	2008	480
973SCSIO1	U1431	2001	48
SO49-017a	U1431	1987	48
973SCSIO2	U1433	2001	48
N3	U1433	?	?
973SCSIO3	ODP1148	2001	48
973SCSIO1	ODP1148	2001	48
Z1		2008	480
O4C1		2004	480
04C2		2004	480

3. Core-Log-Seismic Integration

In this section, we focus primarily on three IODP/ODP sites, IODP Sites U1431 and U1433 in the central basin and ODP Site 1148 in the continental slope, since they provide a complete sedimentary record needed for this study. Sedimentary records from other shallow drill sites (Sites U1432, U1434, and U1435) are also used as references but are not directly presented here.

3.1. Sites U1431 and U1433 in the Central Basin

IODP Expedition 349 drilled five sites in the central SCS basin (Figure 1). Three sites (U1431 in the East Subbasin and U1433 and U1434 in the Southwest Subbasin) reached the oceanic crust. Site U1435 on the northern COB recovered pre-Oligocene sedimentary rocks deposited prior to the opening of the SCS. Furthermore, a full suite of geophysical logging was also carried out at Sites U1431 and U1433 [*Expedition 349 Scientists*, 2014].

Core-log-seismic integration can be carried out in various ways. For example, synthetic seismograms generated from logging data can be compared with seismic data to determine the seismic reflectors that might be associated with certain lithostratigraphic boundaries. In this study, we use the straightforward way of building time-depth conversion equations from *P* wave velocity measurements on cores and then correlate depths in the core to the seismic sequence boundaries as picked in the seismic section based on the time-depth equations.

P wave velocities were measured on working half cores using the *x* axis caliper-type and *z* axis bayonet contact probe transducers on the Section Half Measurement Gantry, and these measurements are in excellent agreement with sonic logging data [*Expedition 349 Scientists*, 2014]. We first apply linear interpolations to these velocity data (Figures 2a and 2c) and then integrate the inverses of interpolated velocity functions with depths at a constant interval of 10 m to obtain the time-depth conversion data pairs, which can be fitted nicely with quadratic polynomial functions (Figures 2b and 2d). At the two deepest sites U1431 and U1433, the quadratic time-depth conversion functions are

$$z = 0.000188295\, t^2 + 0.695896\, t, \quad (1)$$

and

$$z = 0.000152626\, t^2 + 0.714658\, t, \quad (2)$$

respectively. Here t stands for the two-way traveltime starting from the seafloor (TWTT, in milliseconds) and z is the depth in meters below the seafloor (m bsf). Despite their different appearances, equations (1) and (2) are nearly identical numerically (Figure 3). This similarity is remarkable, considering their different tectonic locations and large lithological variations recovered at these two sites. Our further examination confirms that velocity data at the three different sites in the central basin (U1431, U1432, and U1433 in Figure 1) give nearly identical

Table 2. Summary of Mapped Horizons in This Study

Horizon Names	Geological Boundaries	Primary Areal Distribution	Attributes
PP reflector	A prominent reflector above the Pliocene-Pleistocene boundary	Southern East and Southwest Subbasins	Top of the carbonate-rich sequence
Tpp	The Pliocene-Pleistocene boundary	Southern East and Southwest Subbasins	
Tmp	The Miocene-Pliocene boundary	Entire central basin	Sharp change in seismic facies
Tmm	The middle Miocene-late Miocene boundary	Entire central basin	
Tom	The Oligocene-Miocene boundary	Northern continental margin	A major unconformity

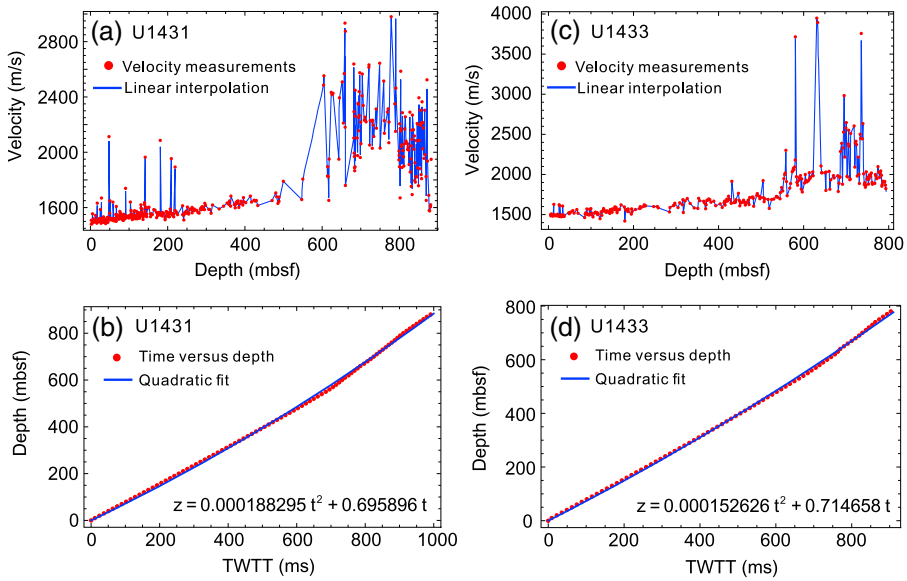

Figure 2. (a and c) *P* wave velocity measurements (red dots) of core samples from Site U1431 in the East Subbasin and U1432 in the Southwest Subbasin, respectively [*Expedition 349 Scientists*, 2014]. Blue lines are linear interpolations between points. (b and d) Calculated data of depth (in meter below seafloor (m bsf) versus two-way traveltime (TWTT, in milliseconds (ms)) starting from the seafloor at Site U1431 and Site U1433, respectively. In the quadratic polynomial fits, *t* stands for TWTT (ms), and *z* is the depth (m bsf).

time-depth relationships, but they deviate gradually but considerably with increasing depths from those obtained at Site U1435 near the COB and ODP Site 1148 located at the continental slope [*Cao et al*., 2014] (Figure 3). This indicates that despite local lithological and velocity variations, time-depth conversion for sediments in the central basin can be well approximated by using a single set of quadratic function, either equation (1) or (2). However, equations (1) and (2) are applicable but only to the central basin floored with oceanic crust. For time-depth conversion at the continental slope, the function obtained from ODP Site 1148 [*Li et al*., 2008] is more appropriate, due to the more consolidated nature and slighter higher velocities of older sediments at depth.

With equation (1) or (2), we can tie depths of major lithostratigraphic boundaries in the cores to the seismic sections. Seismic horizons corresponding to lithostratigraphic boundaries (Table 2) based on the new Geological Time Scale 2012 [*Gradstein et al*., 2012] are picked according to their two-way traveltime estimated from their determined depths at Sites U1431 and U1433 of IODP Expedition 349 (Figures 4 and 5). Sites U1431 and U1433 are located in the East and Southwest Subbasins, respectively. Site U1431 lies to the north of the extinct spreading center, whereas Site U1433 is to the south. Remarkably, the Pliocene/Pleistocene and Miocene/Pliocene age boundaries coincide with characteristic seismic facies boundaries Tpp and Tmp, respectively, confirming the basic principle in seismic stratigraphy that seismic reflections generally indicate isochronous surfaces that do not necessarily correspond to the same lithological contrasts [*Sheriff*, 1980].

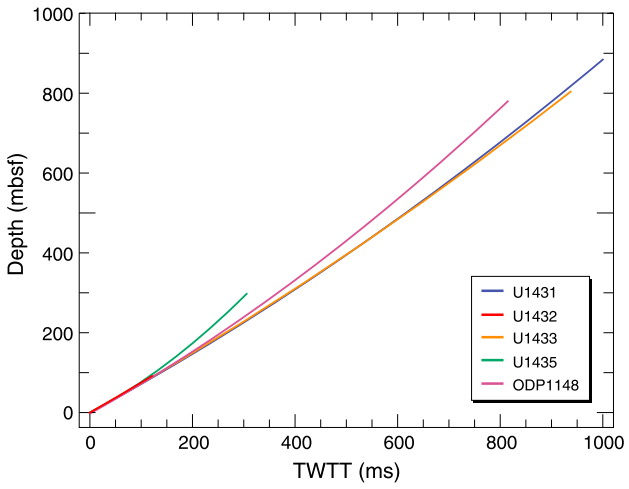

Figure 3. A comparison of depth-time conversion relationships from quadratic polynomial fits of measured velocity data at five different sites.

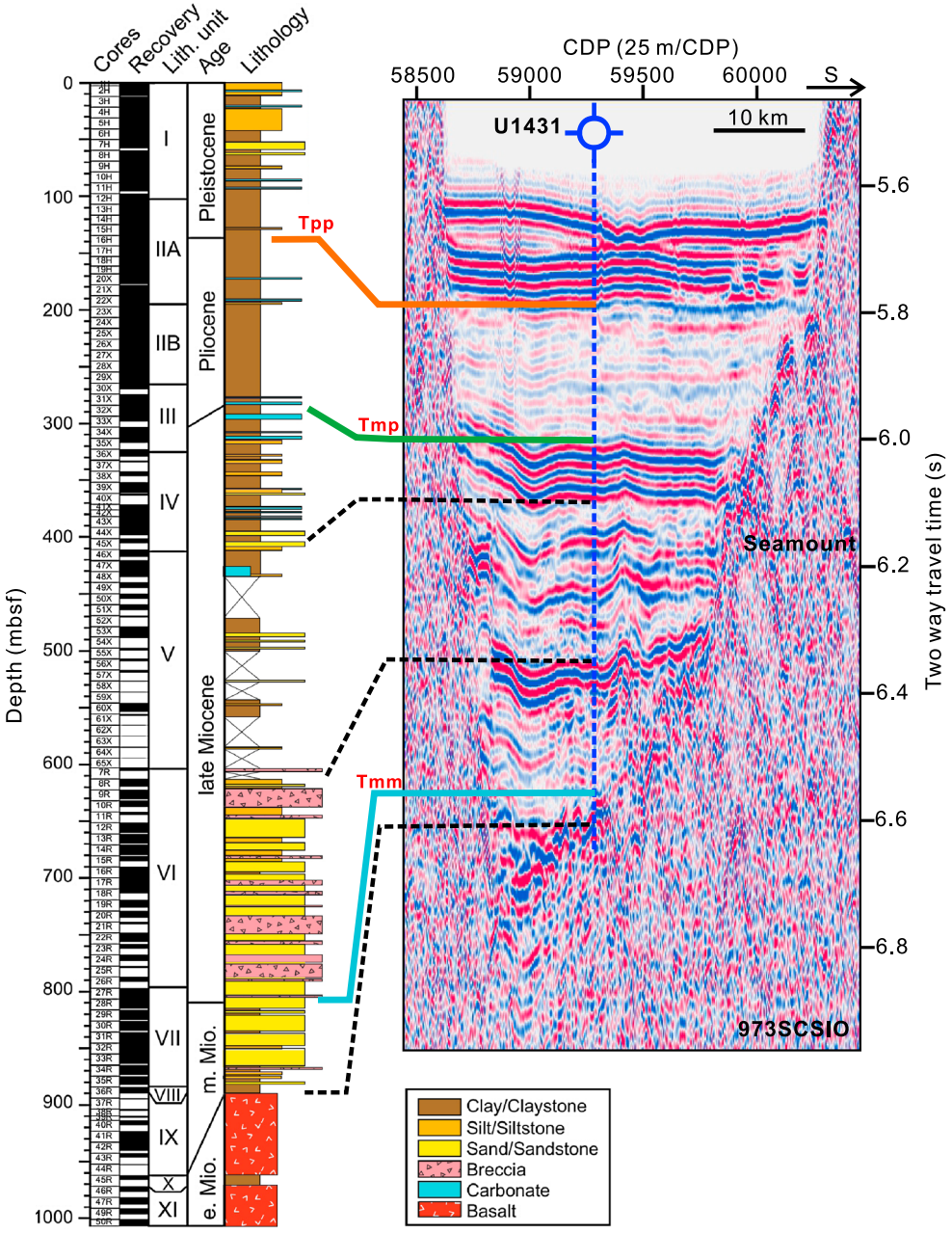

Figure 4. Calibration of seismic horizons from recovered lithostratigraphy at Site U1431 in the East Subbasin. CDP = common depth point.

At Site U1431, we find that the Pleistocene sediments, composed mostly of turbidites, show strong seismic reflectivity. In contrast, the more homogenous Pliocene sediments have much weaker seismic reflectivity (Figure 4), indicating lithological control on acoustic impedance and reflectivity. This control is further manifested in the uppermost units of the upper Miocene (lithostratigraphic units III and IV), where the frequent alternation of lithology between clay, silt, and carbonate causes strong seismic reflectivity, whereas the middle unit of the upper Miocene (lithostratigraphic unit V), composed mainly of poorly consolidated sand causing very low recovery, show weaker reflectivity (Figure 4). The group of strong reflectors in the upper Miocene sequence is caused by the boundary between the middle unit and the lower unit of the upper Miocene (lithostratigraphic unit VI) that has multiple layers of volcanoclastic breccia. The middle Miocene sequence recovered at Site U1431 is composed mainly of sand/sandstone interbedded with

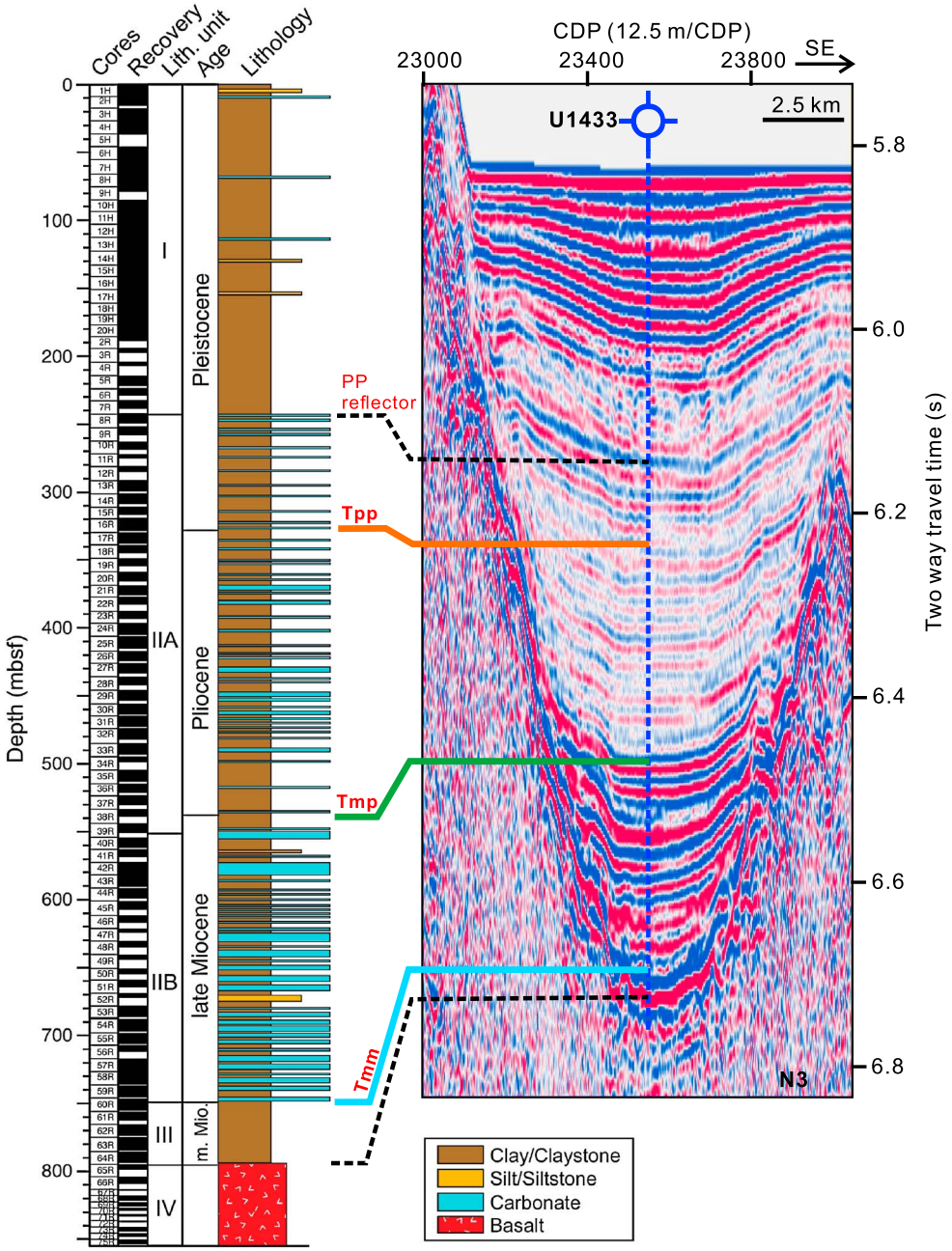

Figure 5. Calibration of seismic horizons from recovered lithostratigraphy at Site U1433 in the Southwest Subbasin. CDP = common depth point.

clay/claystone, with occasional occurrence of thin volcanoclastic breccia layers, and appears more homogenous seismically.

IODP Expedition 349 discovered evident changes in sedimentary facies between Sites U1431 and U1433 [*Expedition 349 Scientists*, 2014]. These changes are also revealed by seismic facies, but some common seismic features remain (Figures 4 and 5). For example, the Pleistocene sediments, although less dominated by turbidite deposition in the upper part at Site U1433, also show strong reflectivity as observed at Site U1431. The lower part of the Pleistocene sediments and the Pliocene sediments at Site U1433 have frequent occurrence of thin carbonate layers, also interpreted as turbidite deposition [*Expedition 349 Scientists*, 2014], but they show weak reflectivity, also similar to what have been observed at Site U1431 for the Pliocene

sequence (Figures 4 and 5). At both sites, the Miocene-Pliocene boundary (Tmp) corresponds to a sharp interface in seismic reflectivity, with weak reflections above and strong reflections below.

One major difference in the Pleistocene sequence between the two sites is that there is an internal boundary between the dominant clay and silt layers (lithostratigraphic unit I) on the top and the alternation between clay and carbonate ooze at the bottom at Site U1433 (top of lithostratigraphic unit IIA) (Figure 5). This lithological boundary has generated a strong seismic reflector (coined as the PP reflector hereafter) above the Pliocene-Pleistocene boundary (Tpp). As will be seen in the next section, this reflector is well developed mostly to the south of the spreading center and becomes more prominent toward the southern continental margin of the SCS.

Another major difference between Sites U1431 and U1433 is the massive presence of lower Pleistocene to upper Miocene carbonate deposition at Site U1433 (Figure 5). The upper Miocene carbonate layers are more abundant and thicker bedded (up to 10 m in maximum thickness) than those in the Pliocene. In addition, the increased consolidation and lithification of the upper Miocene sediment section lead to sharp velocity contrasts and differentiate velocities of different lithologies; lithified carbonates show much higher velocities than interbedded claystone [*Expedition 349 Scientists*, 2014]. These observations explain the strong seismic reflectivity of strata in the bottom unit of the sedimentary cover at Site U1433 (Figure 5).

Pelagic red clay of low-sedimentation rate is recovered immediately above the igneous basement at both Sites U1431 and U1433 [*Expedition 349 Scientists*, 2014]. However, their thicknesses are not over 25 m and are unlikely to be well resolved by surface reflection seismic data. High-resolution seismic survey might be able to map the areal extent for this particular unit.

3.2. ODP Site 1148 in the Continental Slope

ODP Site 1148 is located in the continental slope to the north of the COB (Figure 1). *Li et al.* [2008] also correlated information obtained from cores to seismic reflection data based on the time-depth conversion built at this site. It is shown from this correlation that the Pliocene and Pleistocene sediments at ODP Site 1148, composed mostly of clay [*Wang et al.*, 2000], have similar seismic facies to their deep basin counterparts, respectively. In other words, the Pleistocene sediments have strong seismic reflectivity, whereas the Pliocene sediments show weak reflectivity (Figure 6). Since the Pleistocene sediments vary considerably in composition between sites, but all show quite strong seismic reflectivity, it seems that compaction also plays a major role in modulating seismic reflections in the uppermost sections at studied drill sites.

The upper Miocene sequences show low-frequency and high-amplitude seismic reflection. The lower to middle Miocene sediments have rather chaotic seismic facies compared to sediments above at ODP Site 1148 (Figure 6). This contrast on seismic facies is not observed at Sites U1431 and U1433 in the central basin because the lower to middle Miocene sediments are not well developed there. ODP Site 1148 remains critical for correlating the lower to middle Miocene and older sequences between the continental slope and the old oceanic crust close to the COB. The Oligocene-Miocene boundary (Tom) is characterized by a nondeposition hiatus that correlates to a strong seismic reflector [*Wang et al.*, 2000], and the Oligocene sediments also have rather chaotic seismic facies at ODP Site 1148 (Figure 6).

4. Regional Seismic Stratigraphy

After the core-log-seismic integration at the two key sites in the East and Southwest Subbasins, we can now extrapolate the stratigraphic information from wellbores to the entire central basin by interpreting regional seismic stratigraphy. The area under investigation is rather large, and we find that the seismic facies changes significantly across the extinct spreading center and the Zhongnan Fault. Therefore, to facilitate the discussion, we divide the study area into five subregions, i.e., the continental slope, the northern East Subbasin, the southern East Subbasin, the Southwest Subbasin, and the Northwest Subbasin (Figure 1).

4.1. Northern East Subbasin

This area is located to the north of the fossil ridge and to the east of the interpreted Zhongnan Fault (Figure 1). Figure 7 presents three regional seismic profiles (SO49-017a, 973SCSIO1, and G1) that provide ties in interpreted sequence boundaries in this area. Seismic sections SO49-017a and 973SCSIO1 run

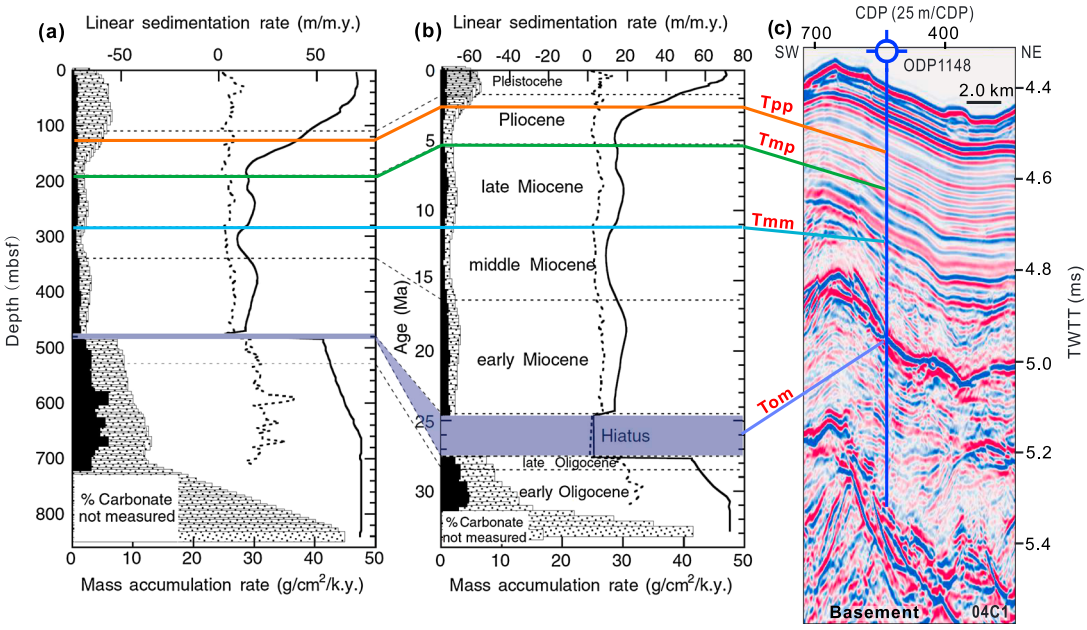

Figure 6. Calibration of seismic horizons with sediments recovered at ODP Site 1148 in the northern continental slope. (a) Linear sedimentation rates (LSR) and mass accumulation rates (MAR) versus depth (m bsf). (b) LSR and MAR versus age. In Figures 6a and 6b, solid curves = total sediment LSR, dashed curves = carbonate LSR, stippled columns = total sediment MAR, and solid columns = carbonate MAR [after *Shipboard Scientific Party*, 2000]. (c) Seismic section 04C1 crossing ODP Site 1148. The black dash line above Tpp is the originally interpreted Pliocene-Pleistocene boundary from ODP Leg 184 [*Wang et al.*, 2000]. The Pliocene-Pleistocene boundary (Tpp) marked in this paper is based on the new Geological Time Scale 2012 [*Gradstein et al.*, 2012]. CDP = common depth point; TWTT = two-way traveltime.

through Site U1431. Close to the fossil ridge, it exists many seamounts and basement highs, which often prevent continuous tracing of seismic horizons, such as on section 973SCSIO1 (Figure 7). But section SO49-017a helps in resolving this problem, allowing straightforward tracing of the Tmp horizon that shows a sharp contrast on seismic reflectivity along the Miocene-Pliocene boundary.

We find that within the northern East Subbasin, seismic facies and sequence boundaries identified at drill site U1431 can be easily traced to other parts, because their features remain fairly consistent, indicating similar abyssal depositional environment and sediment compositions (Figures 7 and 8). For example, the Pliocene sequences are transparent in seismic reflection, compared to strong reflectivity of the Pleistocene sediment above and the Miocene sediments below. The upper Miocene sequences exhibit wavy, mottled, and occasionally chaotic reflections, indicating a relatively high energy environment and quick lateral changes in sedimentary facies. This interpretation is consistent with the recovered upper Miocene sediments with alternating sand and mud layers or composed primarily of sand/sandstone (Figure 4). It is evident from Figure 7 that the top strong reflector of volcanoclastics of Unit VI identified at Site U1431 (Figure 4) is not continuously present in the basin, as previously expected.

Only a thin unit of the middle Miocene sedimentary sequences was recovered at Site U1431, and therefore, the lower to middle Miocene is not very well recovered. Based on the recovered interval, the lithology is mostly sandstone interbedded with thin claystone and occasionally volcanoclastic breccia (Figure 4) [*Expedition 349 Scientists*, 2014]. We expect weak seismic reflectivity for this type of rock formation, at least in the area proximal to Site U1431. This appears to be the case on sections SO49-017a and 973SCSIO1 (Figure 7).

The E-W trending seismic section G1 intersects with sections 973SCSIO1 and SO49-017a at points Ja and Jb, respectively (Figures 1 and 7). From the correlation of seismic horizons, we interpret that the lower to middle Miocene section does show transparent seismic facies in a large part of the northern East Subbasin. However, toward the northern COB, this sequence turns to have high seismic amplitudes (section 973SCSIO1 in Figure 7).

4.2. Northern Continental Slope

Based on the opening model of the SCS [e.g., *Taylor and Hayes*, 1980, 1983; *Briais et al.*, 1993; *C.-F. Li et al.*, 2014], Oligocene sediments are expected in the central basin near the northern COB. Section 973SCSIO1 in

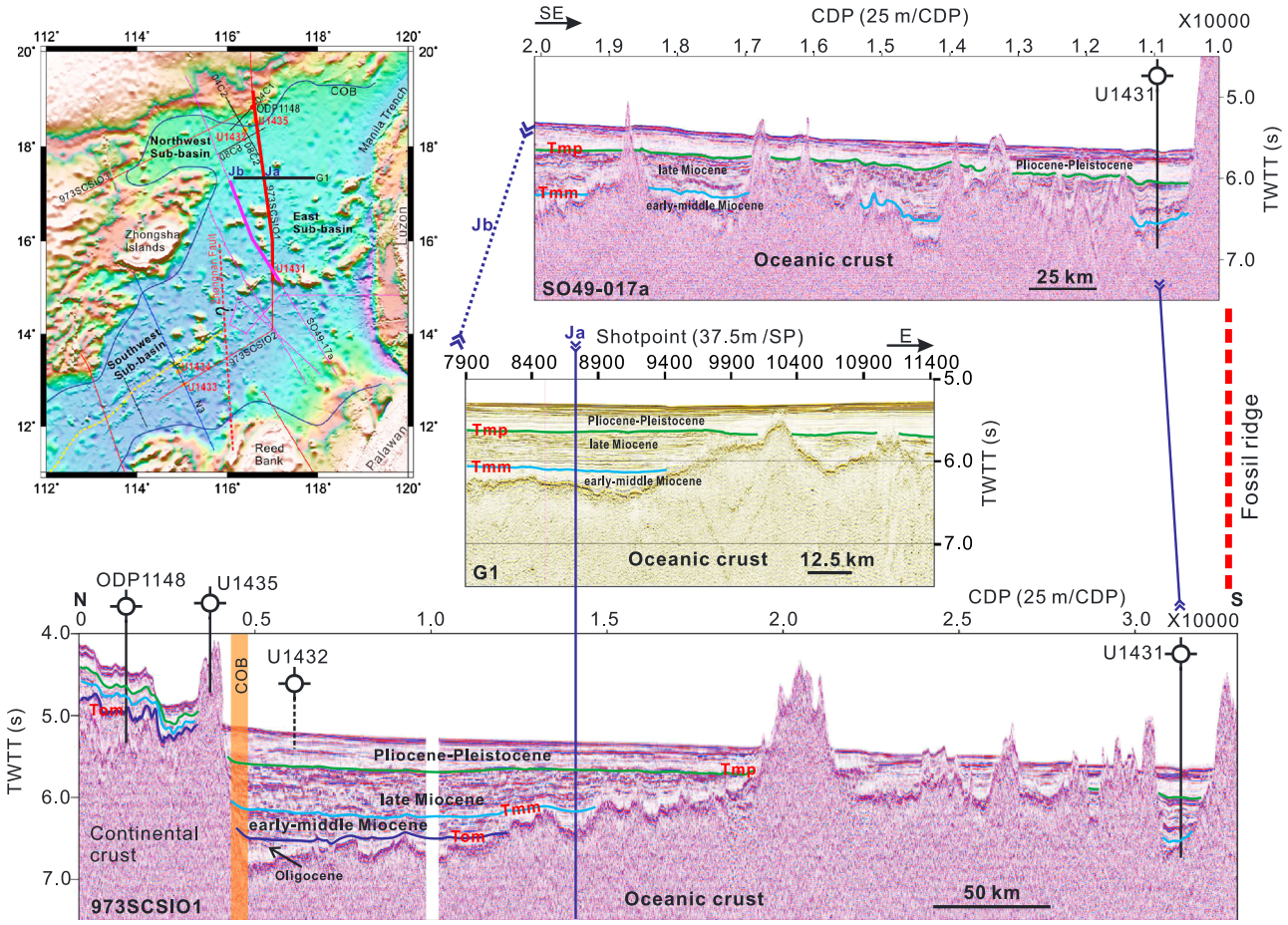

Figure 7. Correlation of seismic sequence boundaries and seismic facies in the northern East Subbasin. Crossing points (Ja and Jb) between seismic sections are marked. The locations of the three seismic sections shown in this figure are highlighted with bold lines in the areal topographic map. COB = continent-ocean boundary, CDP = common depth point, SP = shot point, and TWTT = two-way traveltime.

Figure 7 does not allow a direct comparison on seismic stratigraphy between ODP Site 1148 (where the Oligocene is constrained) and the central basin, because of the basement high developed near the COB. We try to circumvent this problem by studying seismic sections that go around these basement highs and therefore allow direct correlation of the Oligocene from the continental slope to the central basin.

Figure 8 shows seismic sections that provide ties of the Oligocene-Miocene boundary and allow easy tracing of the horizon Tom, because of its characteristically strong seismic reflection. On the two seismic lines of 04C1 and 04C2 that cross with each other, we have noticed that the strong seismic reflectivity of the horizon Tom can be easily traced all the way across the COB from the continental slope to the central basin of the SCS. This allows the correlation of Oligocene sequence.

We find that below the horizon Tom, the deep-marine Oligocene facies changes dramatically, from wavy, chaotic, and strong reflectivity in the continental slope to parallel and transparent seismic facies in the central basin (Figure 8). Based on these seismic characteristics and horizon correlation, we can now interpret the Oligocene sequence on section 973SCSIO1 (Figure 7). The interpreted distribution of the Oligocene in the central basin also helps constrain the age of the oceanic crust. On section 973SCSIO1, the Oligocene sequence pinches out southward, in a location to the north of the seismic section G1 (Figure 7).

These seismic sections near the COB also indicate prolonged compression, faulting, and erosion or depositional hiatus at the Oligocene-Miocene boundary (unconformity Tom) in the continental slope area proximal to the central basin (Figure 8). These late Oligocene to early Miocene exhumation activities in the COB part of the continental margin were probably caused by isostatic uplifting that was associated with the onset of seafloor spreading and continued for several million years, whereas the central basin was in a deep water, quiet

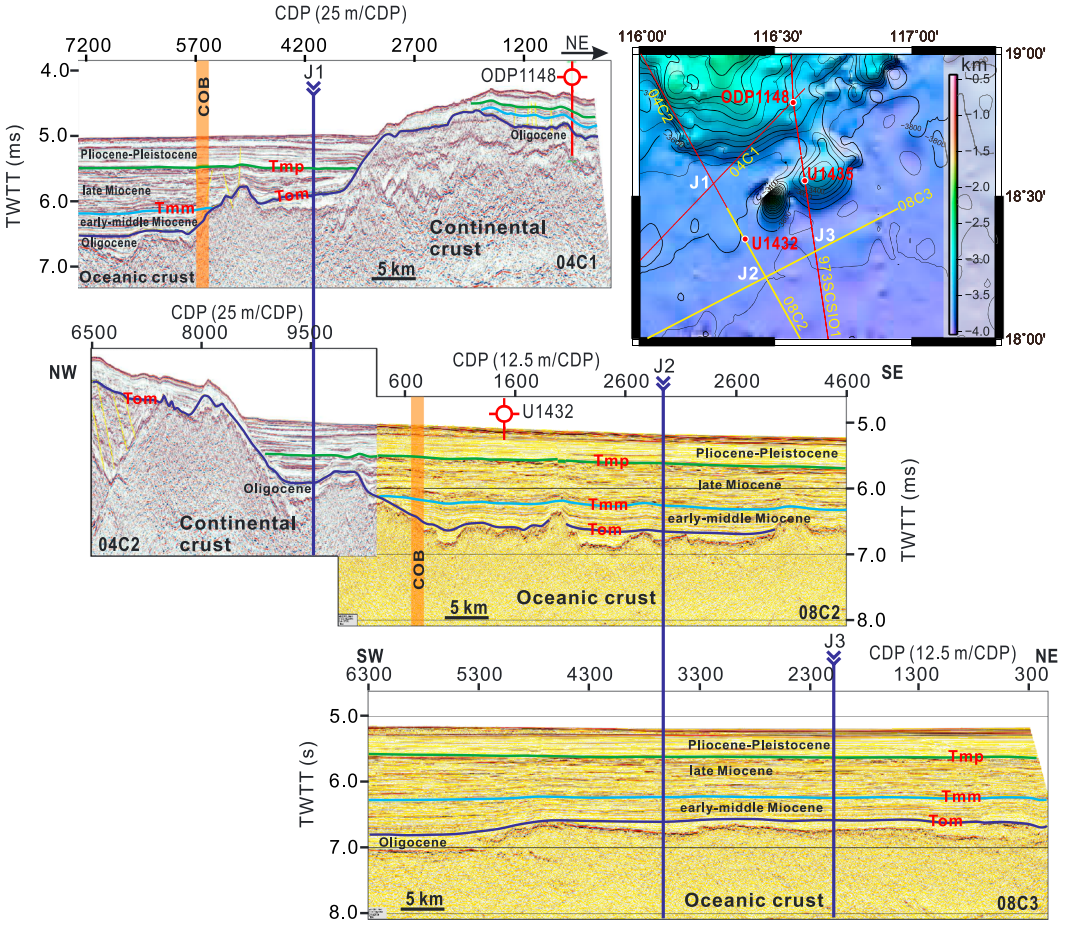

Figure 8. Correlation of seismic sequence boundaries and seismic facies from the continental slope to the northern East Subbasin. Crossing points (J1, J2, and J3) between seismic sections are marked. COB = continent-ocean boundary, CDP = common depth point, and TWTT = two-way traveltime.

depositional environment based on interpreted seismic facies. From seismic stratigraphic correlations (Figures 7 and 8), we can observe that only after the Oligocene did the continental slope and the central basin experience similar subsidence and deep water sedimentation patterns. The sedimentation rates dropped suddenly after the Oligocene at ODP Site 1148 (Figure 6), and more sediments started to transport directly into the central basin.

Seismic section 08C3 intersects with section 973SCSIO1 at point J3 (Figure 8), and other sequence boundaries can be interpreted from horizon ties. Similar seismic facies are observed in Figures 7 and 8 for respective sequences. Site U1432 penetrated only 110 m of Pleistocene clay interbedded with silt and sand [*Expedition 349 Scientists*, 2014]. From this constraint, we know that the Pliocene-Pleistocene boundary (Tpp) near Site U1432 has to be below the base of the recovered section.

4.3. Northwest Subbasin

The Northwest Subbasin forms an east-west elongated embayment to the northwest of the East Subbasin, and is regarded as an abandoned oceanic basin with a very short opening history [*Ru and Pigott*, 1986; *Briais et al*., 1993]. Seismic section 973SCSIO3 passes through ODP Site 1148 and the Northwest Subbasin (Figures 1 and 9). Again, we can trace the strong reflector Tom, the Oligocene-Miocene boundary, from the continental slope to the central basin. Oligocene sequence covers most parts the central basin, except for places with basement highs (Figure 9). Overall, the Oligocene sequence shows weaker seismic reflectivity than the Miocene sequence above, a seismic pattern similar to those found on other seismic profiles in the East Subbasin.

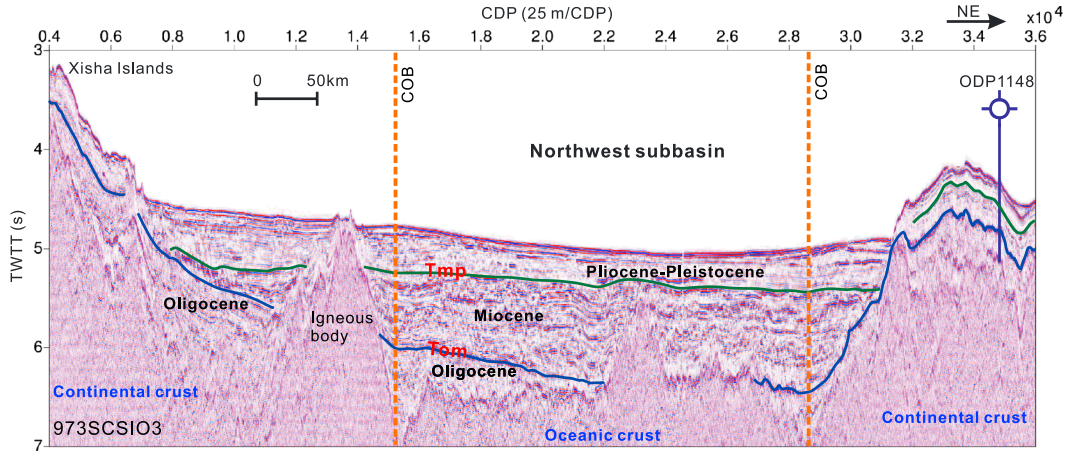

Figure 9. Correlation of seismic sequence boundaries and seismic facies in the Northwest Subbasin. COB = continent-ocean boundary, CDP = common depth point, and TWTT = two-way traveltime.

The Oligocene unit is the thickest near the COB in the Northwest Subbasin, up to 1500 m from our estimate based on equations (1) and (2) and the time interval from the reflection seismic section (Figure 9). This is the thickest Oligocene sequence observed in the entire central basin, indicating earlier rifting/opening of the Northwest Subbasin. However, the distribution of this thick Oligocene sequence is limited to the vicinity of the COB. Elsewhere, its overall average thickness is comparable to that found near the northern margin of the East Subbasin. We therefore assess that the Northwest and East Subbasins started opening nearly at the same time based on seismic stratigraphic correlation.

4.4. Southern East Subbasin

To the south of the fossil ridge of the East Subbasin, there is currently no well control. In addition, there are numerous basement highs that make regional horizon correlation difficult (Figure 10). We find that the seismic sequences constrained by Site U1431 in the northern East Subbasin and by Site U1433 in the Southwest Subbasin cannot be easily traced to the southern East Subbasin, because the extinct spreading ridge and the boundary between the East and Southwest Subbasins (the Zhongnan Fault and Zhongnan Ridge [*Li and Song*, 2012]) acted as major sedimentation boundaries from our interpretation. This can be seen from Figure 10, which shows a large contrast in seismic facies across the fossil ridge. For example, the transparent reflectivity of the Pliocene sequence that is characteristic to the north of the fossil ridge becomes less distinguishable in the southern East Subbasin.

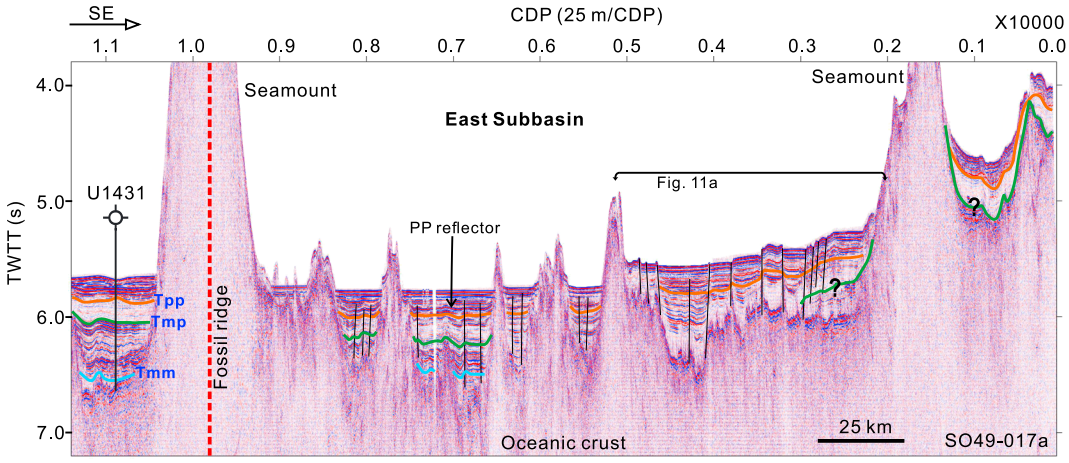

Figure 10. Correlation of seismic sequence boundaries and seismic facies in the southern East Subbasin. Subvertical black line segments are interpreted faults. CDP = common depth point; TWTT = two-way traveltime.

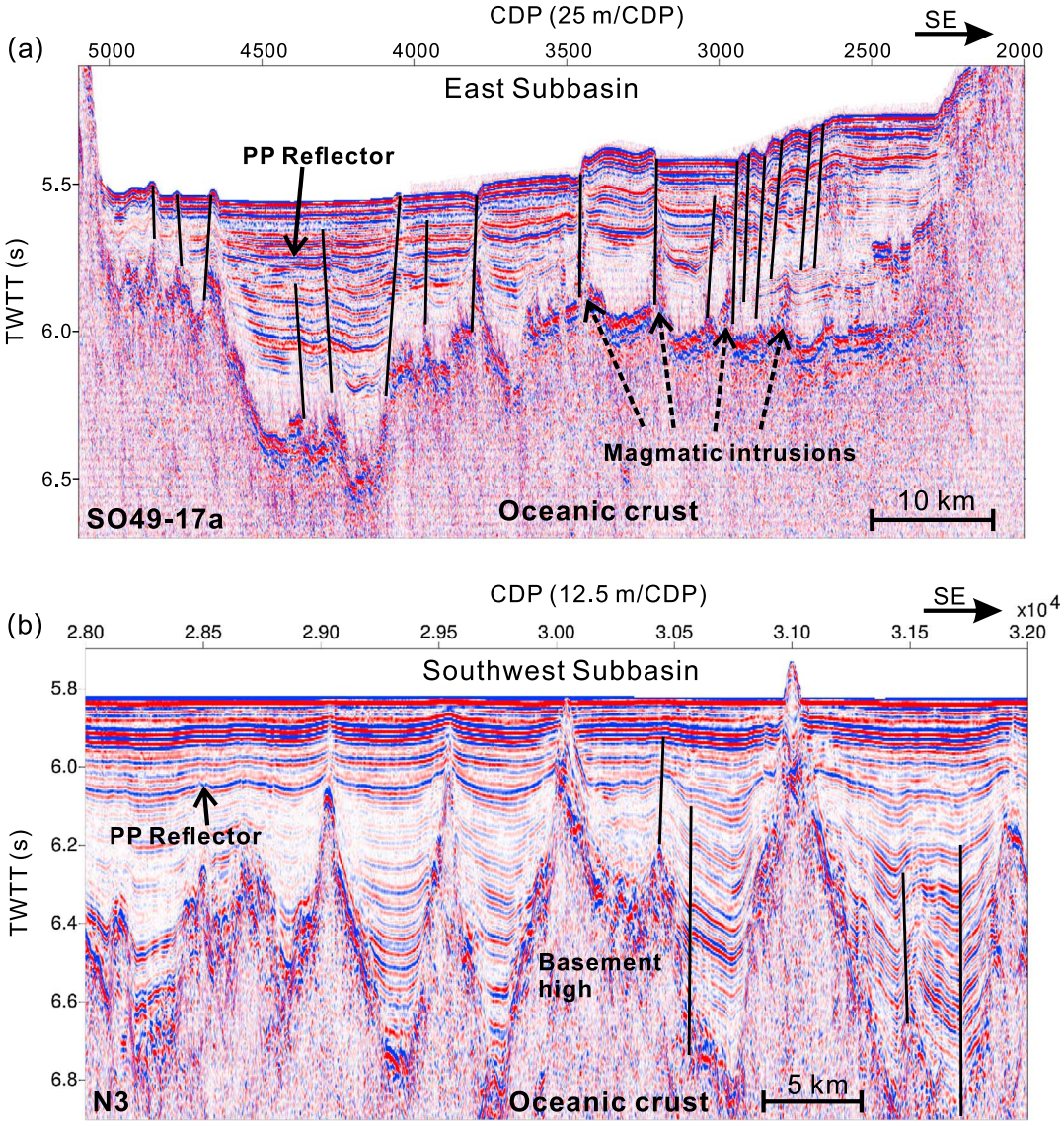

Figure 11. Seismic sections showing the PP reflector, active faults, and magmatic intrusions. (a) Section in the southern East Subbasin. (b) Section in the Southwest Subbasin. Subvertical black line segments are interpreted faults. CDP = common depth point; TWTT = two-way traveltime.

Core-well-seismic integration at Site U1433 identified a prominent reflector (PP reflector) just above the Pliocene-Pleistocene boundary (Tpp) (Figure 5). We find that this PP reflector, showing quite strong seismic reflectivity above the relatively transparent Pliocene sedimentary sequences, is well developed to the south of the fossil ridge, both in the East and Southwest Subbasins (Figures 10 and 11). This PP reflector is used to benchmark our interpreted horizon Tpp beneath it (Figure 10), because from Site U1433, the Pliocene-Pleistoene boundary (Tpp) is just beneath the PP reflector. Compared to the northern East Subbasin, the Pliocene-Pleistocene sediments are thicker, whereas the Miocene sediments, also showing relatively strong seismic reflectivity, are thinner than their northern counterparts.

It is noted that the southern East Subbasin is experiencing active faulting and progressive southward uplifting (Figures 10 and 11a). This intensity in active faulting is not observed to the north of the fossil ridge. Based on the crosscutting relationships, fault activity becomes younger southward to the southern continental margin. Vertical movements along many of these faults have created terraces in the seabed, partly accommodating the progressive southward uplifting (Figures 10 and 11a).

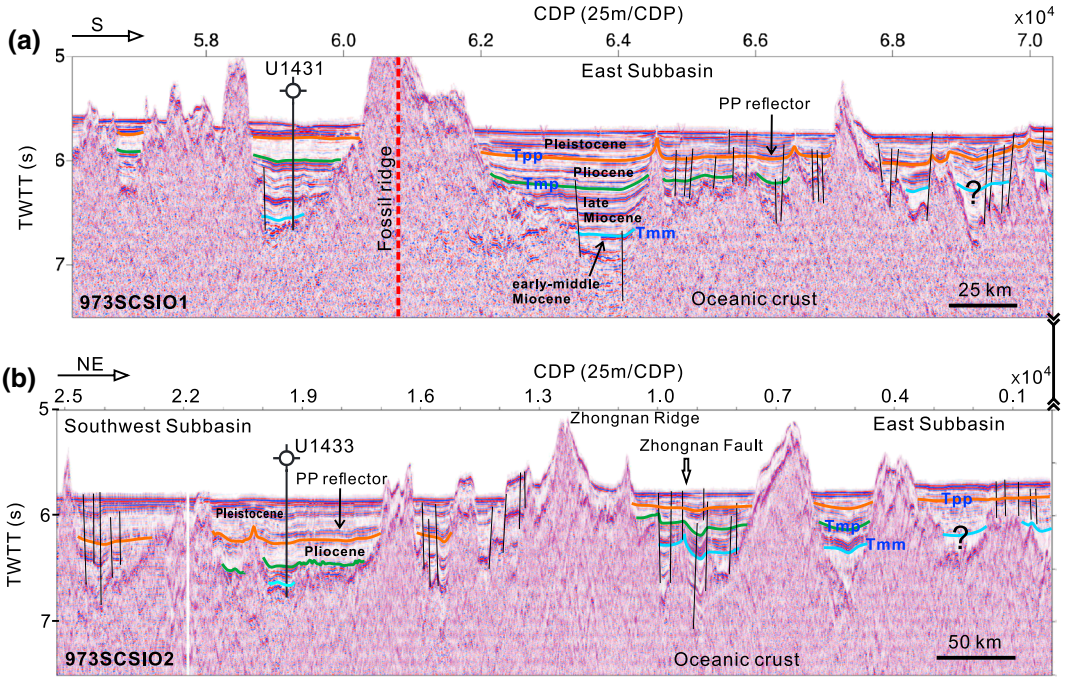

Figure 12. (a) Correlation of seismic sequence boundaries and seismic facies in the East Subbasin. (b) Correlation of seismic sequence boundaries and seismic facies from the Southwest Subbasin to the southern East Subbasin. The two seismic sections join together at their right hand side in the figure. Subvertical black line segments are interpreted faults. CDP = common depth point; TWTT = two-way traveltime.

4.5. Southwest Subbasin

Seismic sections 973SCSIO1 and 973SCSIO2 cross at one end, and together they show large contrasts in seismic facies across the relict spreading center and between the East and Southwest Subbasins (Figures 1 and 12). Subparallel to section SO49-17a (Figure 11), section 973SCSIO1 is also located in the East Subbasin, and the southern segment of section 973SCSIO1 shows many active faults that are progressively younging southward. The Tpp horizon (in orange color) is faulted and the fault steps clearly show recent uplift to the south (Figure 12).

Since sections 973SCSIO1 and 973SCSIO2 are connected, this uplift event seen on section 973SCSIO1 should also be recorded by section 973SCSIO2. On section 973SCSIO2, the interpreted Pleistocene sediments are very thin in the East Subbasin, in sharp contrast to the recovered thick Pleistocene sequence at Site U1433 in the Southwest Subbasin. Similarly, the buried depths of major sequence boundaries and seismic facies also differ markedly. These observations further support the existence of a major tectonic boundary between the two subbasins. Early studies have suggested that the boundary is represented by a major fault called the Zhongnan-Liyue Fault or simply the Zhongnan Fault [*Yao*, 1995; *Li et al*., 2008]. This fault is also characterized as a major boundary in magnetic anomalies [*Li et al*., 2008]. On section 973SCSIO2, we observe that the Zhongnan Fault zone comprises a group of faults, which can reach the seabed as active faults. To the west of the Zhongnan Fault is the Zhongnan Ridge [*Li et al*., 2008; *Li and Song*, 2012], which is subparallel to the Zhongnan Fault and bounded by active faults on both sides (Figures 1 and 12). These structures have played major roles in shaping regional seismic stratigraphy.

Seismic section N3 is nearly perpendicular to section 973SCSIO2 and the two sections intersection at Site U1433 (Figure 13). Section N3 shows very wide hyperextended continental crusts in the conjugate continental margins of the Southwest Subbasin. The PP reflector appears in both the northern and southern parts of the subbasin but is more prominent in the southern part and in the area closer to the southern continental margin (Figure 13). This reflector helps better trace the Pliocene-Pleistocene boundary (Tpp) beneath it. The seismic facies of the Pliocene is similar to what we find elsewhere in the central basin, being rather transparent in seismic reflectivity. We notice that the Pliocene-Pleistocene

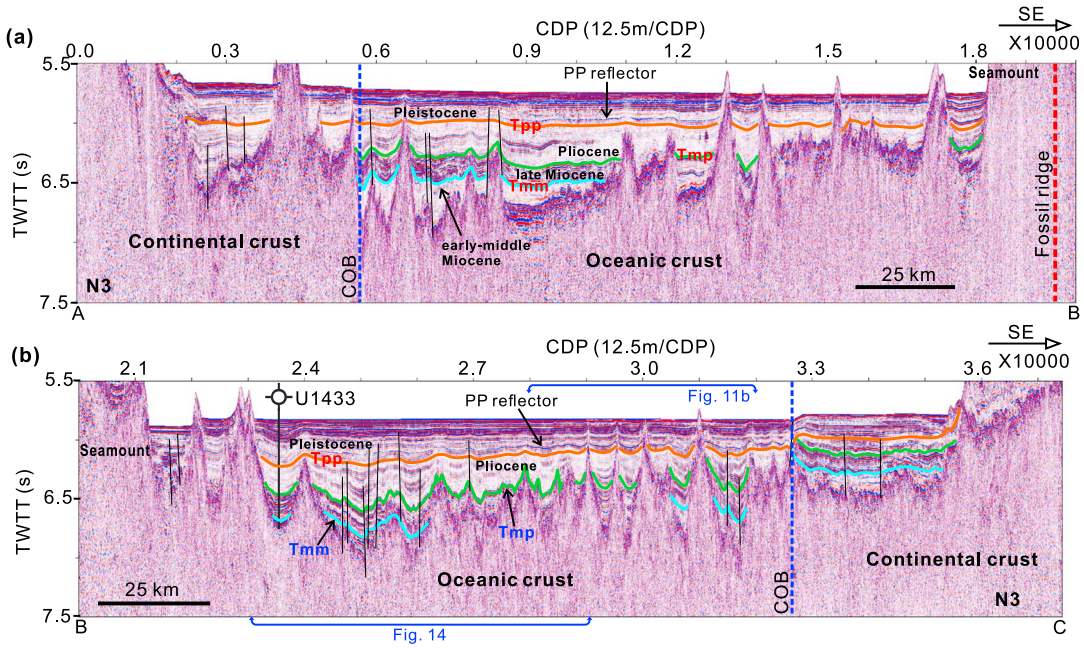

Figure 13. Correlations of seismic sequence boundaries and seismic facies in the Southwest Subbasin. (a and b) To the north and the south of the fossil ridge. Subvertical black line segments are interpreted faults. COB = continent-ocean boundary, CDP = common depth point, and TWTT = two-way traveltime.

sequence is much thicker here than those found elsewhere in the central basin, indicating a higher-sedimentation rate in the Southwest Subbasin since 5 Ma.

The upper Miocene sequence in the Southwest Subbasin has strong seismic reflectivity (Figures 5 and 13), induced by the high velocity of consolidated carbonate layers. Based on this seismic facies, we suggest that this upper Miocene sequence with frequent presence of thick carbonate layers is widespread in the Southwest Subbasin (Figures 13 and 14).

The interpreted lower to middle Miocene differs in seismic facies across the fossil ridge: strong reflection of low frequency to the south of the ridge, but almost transparent reflection to the north (Figure 13). This difference can be explained by drastic differences in sediment supply and/or provenance across the relict spreading center at that time period.

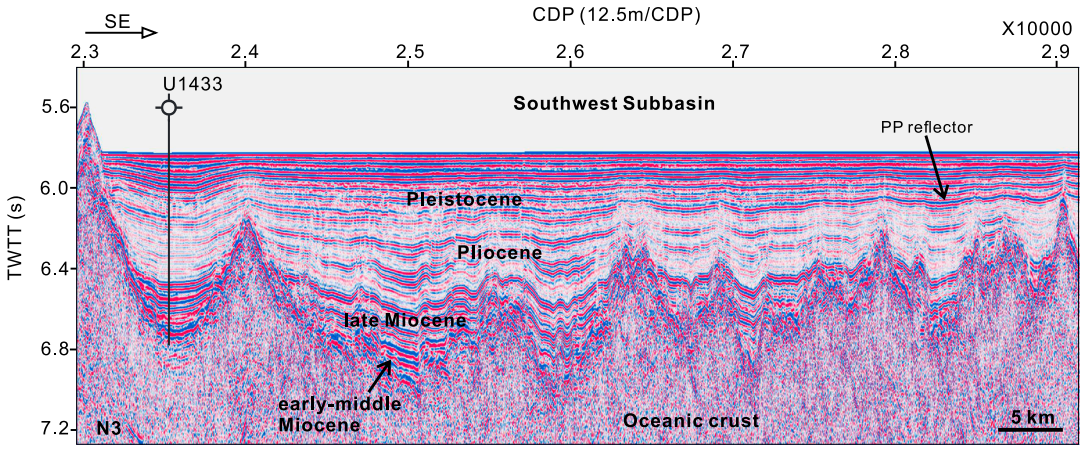

Figure 14. Seismic section showing the distribution of the Miocene facies with strong seismic reflectivity in the Southwest Subbasin. CDP = common depth point; TWTT = two-way traveltime.

5. Implications for Neotectonics

The detailed calibration of seismic sequences makes it possible to examine the timing of neotectonic events in the central SCS basin. In this section, we first discuss the timing of faulting and basement structure formation and then present a summary of the tectonostratigraphic history from seismic stratigraphic analyses.

5.1. Active Faults

The sharp contrast in seismic facies across the Zhongnan Ridge/Fault suggests that it has been active over a long time period. Presently, the Zhongnan Ridge and Fault are still accompanied with active faulting, causing offsets in top basement and seabed (Figure 12b). We find that active faults are more densely developed in the southern East Subbasin (Figures 10–12). This is also the area with uplift occurring progressively southward, as indicated in several seismic sections (Figures 10, 11a, and 12a). Offsets along the active normal faults may have partly accommodated the uplift, because we find that most of these active faults are also associated with offsets or magmatic intrusion in the basement (Figures 10 and 11a). These igneous intrusions, in pinnacle shapes and up to 100 m high, tend to occur where the strong basement reflector is offset by faulting (Figure 11a). Based on the crosscutting relationship between the interpreted intrusions and strata, we estimate that igneous intrusions occurred recently and were accompanied by active faulting in the overlying sediments.

We interpret that this neotectonism in the southern East Subbasin might be caused by the collision of Luzon with Palawan, as well as the subduction of the SCS oceanic lithosphere. Regional bathymetry (Figure 1) shows that the most active subduction (of the SCS lithosphere) or obduction (of Luzon) is occurring in the southern segment of the Manila Trench, where the water depth is the greatest. Earthquake hypocenters also reveal that the downgoing slab is the steepest in this region [e.g., *Bautista et al*., 2001; *Wang et al*., 2014]. This strong convergence along the southeastern margin may have been responsible for active neotectonism in the southeastern part of the central basin. We suggest that the collision progressively lifted the northeast Palawan and the southern part of the southern East Subbasin, causing active normal faults in response to flexural bulging and uplifting.

5.2. Late-Stage Magmatism Versus Basement High

There are many seamounts, igneous intrusions, and basement highs developed in the Southwest Subbasin and in the areas close to the fossil ridge in the East Subbasin. Did they form during seafloor spreading or mostly postspreading? Did they emplace randomly or followed certain temporal or spatial patterns?

As mentioned in section 2, magmatism in the general SCS region experienced three stages, from prerifting stage to rifting and seafloor spreading stage and to postspreading stage that continued into the Quaternary. Previous studies suggested that most volcanic seamounts in the central basin were emplaced after the cessation of seafloor spreading, with a wide age range from as young as ~3.49 Ma to as old as ~13.8 Ma [*Wang et al.,* 1985; *Jin*, 1989]. IODP Expedition 349 also discovered evidences for several million years of postspreading seamount activity along the relict spreading center. At Site U1431, which is near a seamount developed along the relict spreading center of the East Subbasin, IODP Expedition 349 recovered ~280 m of dominantly greenish black volcanoclastic breccia and sandstone, interbedded with minor amounts of claystone (Figure 4) dated to the late middle Miocene to early late Miocene (~8–13 Ma). This would indicate an approximately 5 Myr period of extensive seamount volcanic activity that started nearly 4 Myr after the cessation of seafloor spreading [*Expedition 349 Scientists*, 2014]. At Site U1434, which is near a seamount developed along the relict spreading center of the Southwest Subbasin, this seamount volcanism was not active until ~9 Ma but then was active for at least 2 Myr based on the cored section [*Expedition 349 Scientists*, 2014]. This also puts a time period of ~7 Myr between the cessation of the seafloor spreading and the initiation of seamount activities in the Southwest Subbasin [*Expedition 349 Scientists*, 2014]. This is comparable to late Miocene and Pliocene seamount volcanism found in the extreme southwest of the oceanic basin [*L. Li et al*., 2014].

It is difficult to pinpoint the exact timing of formation of these structures based on seismic stratigraphy alone, because they could have been reactivated by later tectonic events. Here we show various examples that indicate different periods of seamount activity or basement deformation (Figure 15).

Figure 11a already shows young magmatic intrusions associated with active faulting in the southern East Subbasin. In the northern East Subbasin, Figure 15a shows similar active magmatic intrusions that cause

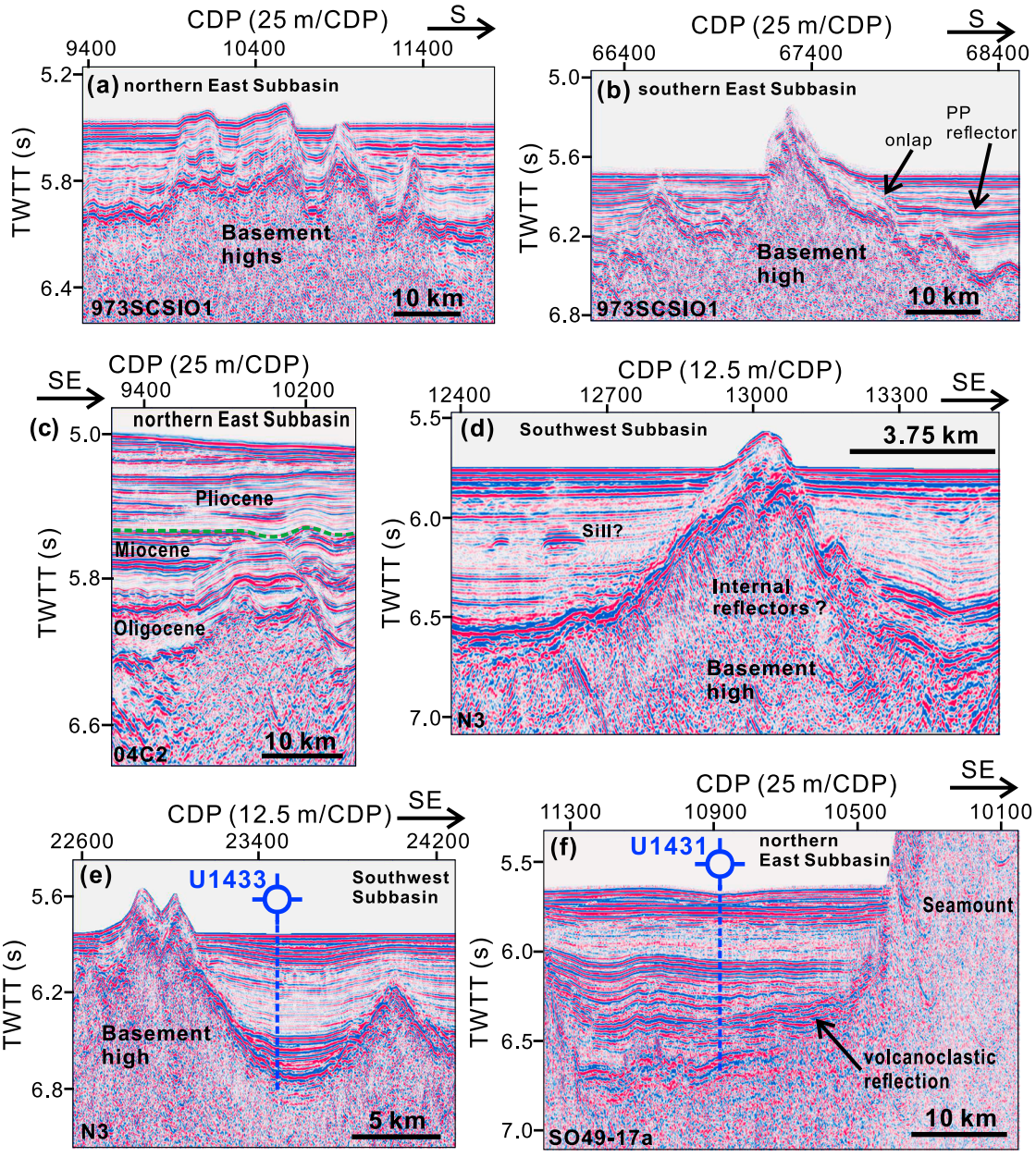

Figure 15. A survey of activity of basement highs, magmatic intrusions, and seamounts revealed by seismic stratigraphy. (a) Active intrusion. (b) Magmatic intrusions activated at about the Pliocene-Pleistocene boundary (~2 Ma). (c) Magmatic intrusions activated at about the middle Miocene to late Miocene boundary (~12 Ma). (d and e) Magmatic intrusions formed during the seafloor spreading. (f) Seismic facies of a volcanoclastic apron caused by the adjacent seamount eruptions in the late Miocene. CDP = common depth point; TWTT = two-way traveltime.

sedimentary offset and deformation above them, but in a very localized segment on seismic section 973SCSIO1. In this case, the seabed and all sediments above the basement are deformed uniformly, indicating very recent magmatic intrusions.

Figure 15b shows magmatic intrusions capped with tilted Pliocene or older sediments, which are then onlapped by Pleistocene sediments. We interpret that this event occurred before the Pleistocene in the southern East Subbasin and could be slightly older than the magmatic intrusions shown in Figure 15a. The deformations shown in Figures 15a and 15b are also similar to those faulting structures found near the Zhongnan Ridge/Fault (between common depth point (CDP) 9000 and 18000 in Figure 12b), all indicating young magmatic and fault activity within the last 5 Ma.

In Figure 15c, a slightly older event is observed close to the northern COB. The basement high has apparently caused uplift of Oligocene and lower to middle Miocene sequences, but younger sediments are in either onlapping or overlying contacts with the deformed older sediments. This suggests a much older event occurred around the middle and the late Miocene boundary.

Many basement highs are also developed in the Southwest Subbasin, some of which are also capped with sediments (Figures 13, 14, 15d and 15e). However, they are not associated with deformation of sediments around them, other than slight tilting related mostly to differential subsidence. In these cases, we interpret them as the basement highs formed during early seafloor spreading, but not late-stage volcanism. Folding and/or tilting of strata on the flanks of these basement highs (Figures 15d and 15e) are more likely caused by differential compression and subsidence, rather than being indicative of later activities. The possible sills of strong reflectivity at ~6.2 s in two-way traveltime on the northwest side of the basement high in Figure 15d are not likely associated with basement high itself. There seem to be regularly tilted internal reflectors within the basement highs that are more indicative of igneous fabrics from seafloor spreading (Figures 15d and 15e), although they could also be noise, out of plane energy, or remnants of diffractions that were not migrated correctly. The absence of volcanoclastic sequence from Site U1433 located in a local depression also supports that the two adjacent basement highs were not from late-stage volcanisms. Otherwise, the recovered sediment cores should have volcanoclastics, as is the case with Site U1431 and U1434 located close to seamounts [*Expedition 349 Scientists*, 2014].

In Figure 15f, we show a typical late-stage volcanic seamount developed in the relict spreading center and its volcanoclastic apron with high seismic reflectivities, caused by interbedding between volcanoclastic breccia and pelagic sediments [*Expedition 349 Scientists*, 2014]. This volcanoclastic facies shows a wedge of volcanoclastic apron that thins away from the seamount to the deeper part of the adjacent local depression and then gradually merges into pelagic clastic facies (Figure 15f).

Overall, we have examined different basement structures and their possible ages of formation or activity. So far we have not observed any periods of pulsed volcanic activity other than strong active tectonics in the southern East Subbasin. Postspreading volcanism appears temporally random based on the data used in this study, but more studies on this topic are needed in the future.

5.3. A Brief Tectonostratigraphic History

During the early opening of the SCS in the Oligocene, the depositional environment in the continental margin proximal to the oceanic lithosphere differs markedly from that in the central basin. This is seen in seismic facies that are often chaotic and of high seismic amplitude in the continental slope but transparent and parallel in the deep basin (Figures 7–9). Many parts of the continental slope experienced differential uplift and erosion, causing the strong Tom reflector along the Oligocene-Miocene boundary (Figures 7–9 and 16). In places between half grabens in the northern continental margin (seismic section 04C2 in Figure 8), the Tom reflector is merged with the breakup unconformity [*Li et al*., 2010], which can be identified in the grabens in the northern margin and is caused by the onset of seafloor spreading and the final breakup of the continental lithosphere around 33 Ma [*Expedition 349 Scientists*, 2014; *C.-F. Li et al*., 2014]. This suggests a long depositional hiatus that forms the Tom unconformity. Only after the Oligocene did similar deep-marine depositional settings and seismic facies start to occur from the continental slope to the central basin.

The wavy, mottled, and occasionally chaotic Miocene facies in most parts of the central basin indicate rapid changes in lithology, both spatially and temporally. The early to middle Miocene is also a period of active seafloor spreading and rapid thermal subsidence (Figure 16), which in turn provided large accommodation spaces for accelerated erosion in the continental margin [e.g., *Taylor and Hayes*, 1980, 1983; *Briais et al*., 1993; *C.-F. Li et al*., 2014]. Large volumes of terrestrial clastic materials, and carbonate materials from surrounding carbonate banks around the Southwest Subbasin, were transported rapidly into the central basin via turbidity currents (Figure 16). These turbidite deposits are found in all sites cored during IODP Expedition 349 [*Expedition 349 Scientists*, 2014], indicating widespread turbidity current activity in the SCS. This strong and frequent mixing of sediments of different sources causes this characteristic Miocene seismic facies. Only in areas farther away from the margins and closer to the spreading center are found more transparent lower to middle Miocene seismic facies indicative of relatively quiet abyssal sedimentary environment.

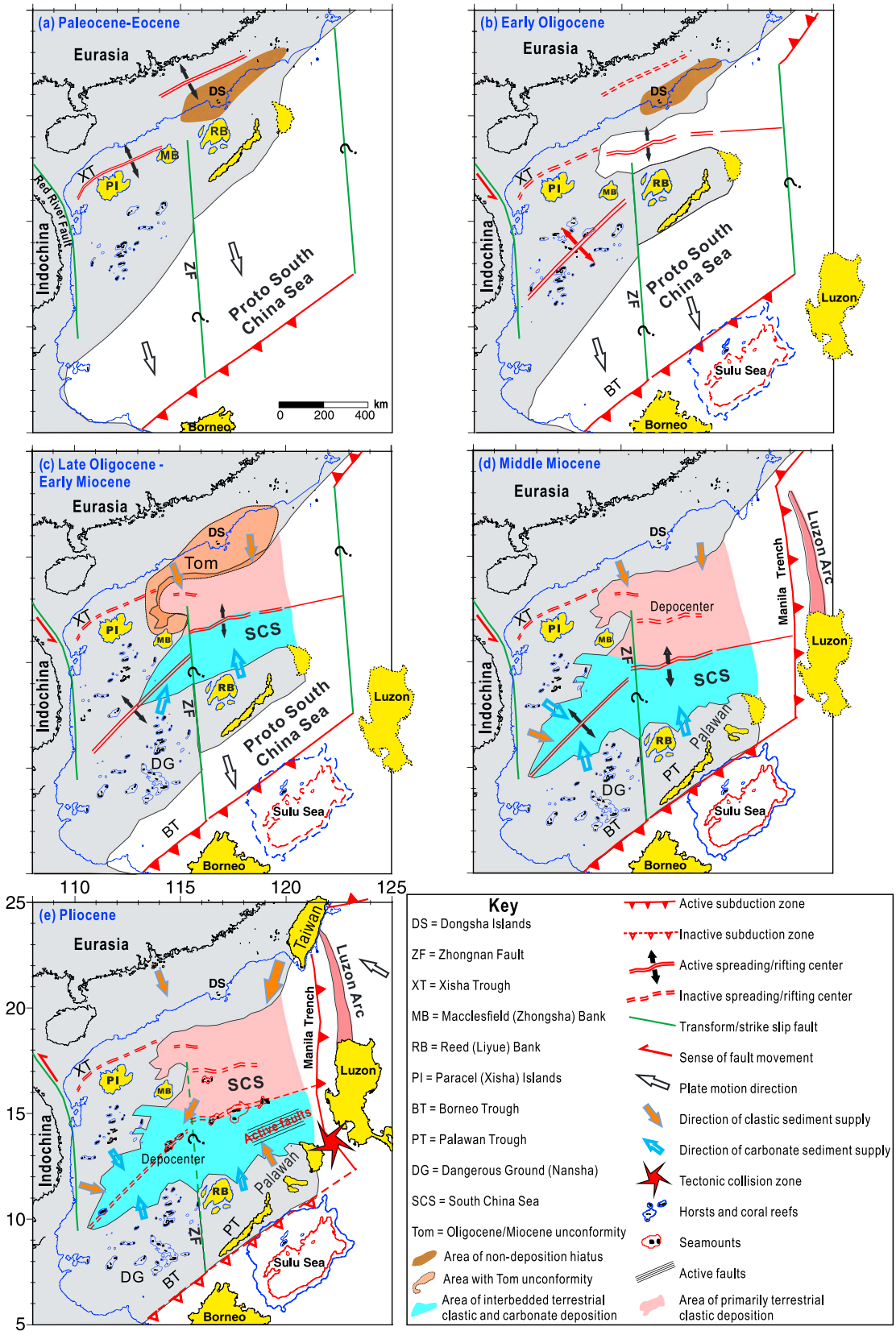

Figure 16. Cenozoic tectonostratigraphic evolution of the South China Sea. Note that this summarizing model is a drastic modification to the early model of *Li et al.* [2007], which incorrectly suggested that the Southwest Subbasin opened earlier than the East Subbasin.

In many parts of the central basin, the Pliocene sequence is drastically different from the underlying Miocene sequences, as it is a rather homogeneous seismic facies. This forms a sharp contrast in seismic sections, indicating a major tectonic event or a change in regional sedimentary environment that occurred around 5 Ma. This timing corresponds to the onset of accelerated subsidence in the northern continental margin [e.g., *Su et al*., 1989; *Clift and Lin*, 2001], the buildup of the Taiwan Orogen [e.g., *Biq*, 1972; *Chai*, 1972; *Teng*, 1990; *Huang et al*., 2001], and the shift from left-lateral to right-lateral strike-slip movement along the Red-River Fault [e.g., *Rangin et al*., 1995; *Clift and Sun*, 2006; *Zhu et al*., 2009]. Rapid submergence of a large part of the northern continental margin led to different sediment sources and longer transport distances for sediments to be deposited in the central basin, and this could explain the Pliocene seismic facies more characteristic of a quiet deep water environment. It also seems likely that the Taiwan Orogen is a major provenance for post-Miocene sediments in the SCS basin [*Expedition 349 Scientists*, 2014]. Therefore, we suggest that the seismic facies in the central SCS basin responded evidently to these major regional tectonic events.

An exception to this is found in the southern East Subbasin, where the Pliocene reflectivity is less transparent (Figures 10 and 12). We interpret that this indicates quite different sediment sources across the fossil ridge of the SCS; instead of coming mostly from the northern continental margin, here in the southern East Subbasin the Pliocene terrigenous and carbonate sediments are expected mostly from southern lands [*Expedition 349 Scientists*, 2014] (Figure 16).

Thick upper Miocene sequence is discovered at Site U1431 in the northern East Subbasin, but Site U1433 to the south of the fossil ridge in the Southwest Subbasin revealed much thinner upper Miocene but much thicker Pleistocene sediments (Figure 12). Our regional seismic interpretation indicates that the information revealed by these two sites are very representative of the respective subregions where they are located. These basin-wide observations suggest that the subbasin or place with the fastest sedimentation rate in the central basin has changed. During the late Miocene, the fastest sedimentation occurred in the northern East Subbasin, probably linked at least partially to sufficient sediment supply from the northern continental margin. Since the Pliocene, the Southwest Subbasin and the area close to the fossil ridge in the southern East Subbasin have started to have the largest sedimentation rates (Figure 16). This sedimentary pattern and trend since the Pliocene continue today, and correspondingly, the present bathymetry shows that the Southwest Subbasin and the area close to the fossil ridge in the southern East Subbasin have the deepest water depth, forming the present-day depocener in the SCS (Figure 1).

Since the PP reflector we identified at Site U1433 represents a lithological boundary between primarily clay above and interbedded clay and carbonate beneath (Figure 5), the areal distribution of the reflector can be used to estimate the presence of carbonate turbidite deposition. The PP reflector, showing high seismic amplitudes, is best developed to the south of the fossil ridge of the SCS (Figures 10–14), can be identified in the northern Southwest Subbasin (Figure 13), but is mostly absent or unidentifiable in the northern East Subbasin (Figures 7–9). Taken together with recovered lithologies from IODP Expedition 349 [*Expedition 349 Scientists*, 2014], we estimate that Miocene-Pliocene carbonate turbidites are extensively developed in the Southwest and the southern East Subbasins, but not in the Northwest and northern East Subbasins (Figure 16). This can be explained by the fact that Southwest and the southern East Subbasins are more proximal to southern blocks, such as the Reed Bank, the Palawan, and the Dangerous Ground, which were largely capped with carbonate [e.g., *Hutchison and Vijayan*, 2010; *Franke et al*., 2011; *Yao et al*., 2012; *Ding et al*., 2013], and could have supplied carbonate materials into the basin via turbidity currents [*Expedition 349 Scientists*, 2014].

6. Conclusion

In this study, we have analyzed a large volume of reflection seismic data, collected over the years by various research institutions in the central SCS basin, and interpreted major seismic sequence boundaries through integration with cores collected during recent IODP Expedition 349. We interpret first-order sequence boundaries throughout the basin, which are Oligocene/Miocene, middle Miocene/upper Miocene, Miocene/Pliocene, and Pliocene/Pleistocene boundaries. Characteristic seismic reflectors are also examined. Seismic facies in the central basin and the proximal continental slope are analyzed to infer changes in sedimentary environment, provenance, and also magmatism. All together we draw the following major conclusions:

1. Rapid spatial and temporal variations in seismic facies are evident across subbasin boundaries in the SCS basin, although within each subbasin, the seismic facies are more consistent laterally. However, time-depth conversion relationships for sediments constructed from velocity measurements of recovered cores from Sites U1431, U1432, and U1433 in the central basin are nearly identical but differ from those at Sites U1435 and ODP 1148 in the northern continental slope. This puts more confidence on areal stratigraphic correlation in the central basin. More remarkable but theoretically correct is that some biolithological boundaries identified from IODP Expedition 349 coincide well with certain characteristic seismic horizons (Figures 4 and 5).
2. Despite variation in seismic facies across the fossil spreading ridge, the Pliocene sequence is mostly characterized by very weak and parallel seismic reflectivity, often in large contrasts to the strong and parallel Pleistocene seismic reflectivity above and wavy, subparallel, and mottled Miocene seismic facies beneath. The sharp change in seismic facies at about the Miocene-Pliocene boundary indicates that a dramatic tectonostratigraphic event occurred around the SCS at about 5 Ma, coeval with major tectonic events such as the uplift of the Taiwan Orogen, accelerated subsidence and transgression in the northern continental margin, and the reversal in strike-slip movement along the Red-River Fault. The discovered Oligocene sequences in the central basin appear in weak seismic reflectivity, but this seismic facies differs from the often strong and chaotic Oligocene seismic facies in the continental slope.
3. Sharp contrasts in seismic facies are observed across the fossil ridge and across the Zhongnan Ridge/Fault between the East and Southwest Subbasins, indicating that these structures worked as major sediment barriers and that long-term tectonic activity has occurred around the Zhongnan Ridge/Fault. The Pliocene seismic facies also changes slightly across the fossil ridge.
4. Massive Miocene carbonate deposition with strong seismic reflectivity is identified in the Southwest Subbasin. Furthermore, based on the identified early Pleistocene PP reflector that separates clay above and interbedded clay and carbonate beneath at IODP Site U1433, we suggest that Miocene and Pliocene carbonate deposits are widely distributed in the Southwest and southern East Subbasins, but not in the northern East Subbasin. The Southwest and southern East Subbasins are surrounded by southern blocks that are preferentially capped with carbonates, which provide carbonate materials that are then transported by turbidity currents into the central basin. The northern East Subbasin, however, received sediments primarily from the north with much less Miocene carbonate development.
5. The subbasin of the largest sedimentation rate switched from the northern East Subbasin during the Miocene to the Southwest Subbasin and the area close to the fossil ridge in the southern East Subbasin in the Pleistocene. The present-day bathymetry of the SCS also shows the largest water depths at these areas with the highest Pleistocene sedimentation rate.
6. The most active faulting now occurs in the southern East Subbasin, caused most likely by the active and fastest subduction/obduction in the southern segment of the Manila Trench and the collision between the Northeast Palawan and the Luzon arc. This tectonic force is also responsible for progressive southward uplifting in the southern East Subbasin.
7. Timing and seismic facies related to formation and/or activity of oceanic spreading and postspreading volcanic activity, including seamounts and magmatic intrusions, are surveyed based on the seismic data presented in this paper. Their various ages can be determined approximately in light of interpreted seismic stratigraphy, and we find no temporal clustering in their activity/formation.

Acknowledgments

This research is funded by National Science Foundation of China (grants 91428309 and 91028007), Program for New Century Excellent Talents in University, and Research Fund for the Doctoral Program of Higher Education of China (grant 20100072110036). This research also used samples and/or data provided by the International Ocean Discovery Program (IODP). We thank the officers, technician, engineers, and crew members of D/V *JOIDES Resolution* for their critical contributions. Data processing and mapping is supported by GMT [*Wessel and Smith*, 1995] and Seismic Unix [*Cohen and Stockwell*, 2002]. We also thank Ryan Lester, an anonymous reviewer, and the Associate Editor for their very detailed review and helpful comments. Data related to IODP Expedition 349 will be available for downloading from the IODP website (www.iodp.org) after the moratorium period, which will end on 30 March 2015. Reflection seismic data are from State Key Laboratory of Marine Geology, Tongji University; Second Institute of Oceanography, State Oceanic Administration, China; Federal Institute for Geosciences and Natural Resources, Hannover, Germany; Guangzhou Marine Geological Survey, China; and China National Offshore Oil Company Ltd.

References

Barckhausen, U., M. Engels, D. Franke, S. Ladage, and M. Pubellier (2014), Evolution of the South China Sea: Revised ages for breakup and seafloor spreading, *Mar. Pet. Geol.*, *58*, 599–611, doi:10.1016/j.marpetgeo.2014.02.022.

Bautista, B. C., M. L. P. Bautista, K. Oike, F. T. Wu, and R. S. Punongbayan (2001), A new insight on the geometry of subducting slabs in northern Luzon, Philippines, *Tectonophysics*, *339*, 279−310.

Biq, C. C. (1972), Transcurrent buckling, transform faulting and transpression, their relevance in eastern Taiwan kinematics, *Pet. Geol. Taiwan*, *20*, 1–39.

Briais, A., P. Patriat, and P. Tapponnier (1993), Updated interpretation of magnetic anomalies and seafloor spreading stages in the South China Sea: Implications for the Tertiary tectonics of Southeast Asia, *J. Geophys. Res.*, *98*, 6299–6328, doi:10.1029/92JB02280.

Cao, Y., C.-F. Li, T. Williams, A. Briais, H. S. Trinh, Y.-C. Yeh, F. Zhang, and Expedition 349 Scientists (2014), Tectonic subsidence of the East Subbasin of the South China Sea, Abstract T33C-4697 presented at 2014 Fall Meeting, AGU, San Francisco, Calif.

Chai, B. H. (1972), Structure and tectonic evolution of Taiwan, *Am. J. Sci.*, *272*, 389–432.

Chung, S. L., S. Sun, K. Tu, C. H. Chen, and C. Lee (1994), Late Cenozoic basaltic volcanism around the Taiwan Strait, SE China: Product of lithosphere-asthenosphere interaction during continental extension, *Chem. Geol.*, *112*(1–2), 1–20.

Chung, S. L., H. Cheng, B.-M. Jahn, S. Y. O'Reilly, and B. Zhu (1997), Major and trace element, and Sr-Nd isotope constraints on the origin of Paleogene volcanism in South China prior to the South China Sea opening, *Lithos*, *40*, 203–220.
Clift, P., and J. Lin (2001), Preferential mantle lithospheric extension under the South China margin, *Mar. Pet. Geol.*, *18*, 929–945.
Clift, P. D., and Z. Sun (2006), The sedimentary and tectonic evolution of the Yinggehai-Song Hong basin and the southern Hainan margin, South China Sea: Implications for Tibetan uplift and monsoon intensification, *J. Geophys. Res.*, *111*, B06405, doi:10.1029/2005JB004048.
Cohen, J. K., and J. W. Stockwell Jr. (2002), CWP/SU: Seismic Un*x Release No. 36: An open source software package for seismic research and processing, Center for Wave Phenomena, Colorado School of Mines.
Ding, W., D. Franke, J. Li, and S. Steuer (2013), Seismic stratigraphy and tectonic structure from a composite multi-channel seismic profile across the entire Dangerous Grounds, South China Sea, *Tectonophysics*, *582*, 162–176.
Expedition 349 Scientists (2014), South China Sea tectonics: Opening of the South China Sea and its implications for southeast Asian tectonics, climates, and deep mantle processes since the late Mesozoic, *International Ocean Discovery Program Preliminary Report*, 349, doi:10.14379/iodp.pr.349.2014.
Franke, D., U. Barckhausen, N. Baristeas, M. Engels, S. Ladage, R. Lutz, J. Montano, N. Pellejera, E. G. Ramos, and M. Schnabel (2011), The continent–ocean transition at the southeastern margin of the South China Sea, *Mar. Pet. Geol.*, *28*(6), 1187–1204.
Gradstein, F. M., J. G. Ogg, M. D. Schmitz, and G. M. Ogg (coordinators) (2012), *The Geologic Time Scale 2012*, vol. 2, 1176 pp., Elsevier, Boston, plus chart.
Hall, R. (2002), Cenozoic geological and plate tectonic evolution of SE Asia and the SW Pacific: Computer-based reconstructions, model and animations, *J. Asian Earth Sci.*, *20*, 353–431.
Han, X. Q. (2011), Ocean ridge basalt of Southwestern Subbasin in the South China Sea: Rock geochemistry and geochronology constraints of South China Sea, "South China Sea Deep" Annual Meeting abstract S1-O-12 [in Chinese]. Shanghai, 26–27.
Hsu, S.-K., Y.-C. Yeh, W.-P. Doo, and C.-H. Tsai (2004), New bathymetry and magnetic lineations identifications in the northernmost South China Sea and their tectonic implications, *Mar. Geophys. Res.*, *25*, 29–44.
Huang, C.-Y., K.-Y. Xia, P. B. Yuan, and P.-G. Chen (2001), Structural evolution from Paleogene extension to Latest Miocene-Recent arc-continent collision offshore Taiwan: Comparison with on land geology, *J. Asian Earth Sci.*, *19*, 619−639.
Hutchison, C. S., and V. R. Vijayan (2010), What are the Spratly Islands?, *J. Asian Earth Sci.*, *39*, 371–385.
Jin, Q. (1989), *Geology and Hydrocarbon Resources of the South China Sea* [in Chinese], 417 pp., Geological Publishing House, Beijing.
Koppers, A. A. P., and Expedition 349 Scientists (2014), On the $^{40}Ar/^{39}Ar$ dating of low-potassium ocean crust basalt from IODP Expedition 349, South China Sea, Abstract T31E-03 presented at 2014 Fall Meeting, AGU, San Francisco, Calif.
Kudrass, H. R., M. Hiedicke, P. Cepek, H. Kreuzer, and P. Müller (1986), Mesozoic and Cenozoic rocks dredged from the South China Sea (Reed Bank area) and Sulu Sea and their significance for plate-tectonic reconstructions, *Mar. Pet. Geol.*, *3*, 19–30.
Li, C.-F., and T. R. Song (2012), Magnetic recording of the Cenozoic oceanic crustal accretion and evolution of the South China Sea basin, *Chin. Sci. Bull.*, *57*, 3165–3181.
Li, C.-F., Z. Zhou, J. Li, H. Hu, and J. Geng (2007), Structures of the northeasternmost South China Sea continental margin and ocean basin: Geophysical constraints and tectonic implications, *Mar. Geophys. Res.*, *28*, 59–79.
Li, C.-F., Z. Zhou, J. Li, B. Chen, and J. Geng (2008), Magnetic zoning and seismic structure of the South China Sea ocean basin, *Mar. Geophys. Res.*, *29*, 223–238.
Li, C.-F., X. Shi, Z. Zhou, J. Li, J. Geng, and B. Chen (2010), Depths to the magnetic layer bottom in the South China Sea area and their tectonic implications, *Geophys. J. Int.*, *182*, 1229–1247.
Li, C.-F., J. Lin, and D. K. Kulhanek (2013), South China Sea tectonics: Opening of the South China Sea and its implications for southeast Asian tectonics, climates, and deep mantle processes since the late Mesozoic, *IODP Sci. Prosp.*, *349*, doi:10.2204/iodp.sp.349.2013.
Li, C.-F., et al. (2014), Ages and magnetic structures of the South China Sea constrained by deep tow magnetic surveys and IODP Expedition 349, *Geochem. Geophys. Geosys.*, *15*, 4958–4983, doi:10.1002/2014GC005567.
Li, L., P. D. Clift, R. Stephenson, and H. Nguyen (2014), Non-uniform hyper-extension in advance of seafloor spreading on the Vietnam continental margin and the SW South China Sea, *Basin Res.*, *26*, 106–134.
Li, Z. X., and X. H. Li (2007), Formation of the 1300 km-wide intra-continental orogen and post-orogenic magmatic province in Mesozoic South China: A flat-slab subduction model, *Geology*, *35*, 179–182.
Liu, W.-N., C.-F. Li, J. Li, D. Fairhead, and Z. Zhou (2014), Deep structures of the Palawan and Sulu Sea and their implications for opening of the South China Sea, *Mar. Pet. Geol.*, *58*, 721–735.
Lüdmann, T., and H. K. Wong (1999), Neotectonic regime at the passive continental margin of the northern South China Sea, *Tectonophysics*, *311*, 113–138.
Lüdmann, T., H. K. Wong, and P. Wang (2001), Plio-Quaternary sedimentation processes and neotectonics of the northern continental margin of the South China Sea, *Mar. Geol.*, *172*, 331–356.
Rangin, C., M. Klein, D. Roques, X. Le Pichon, and L. V. Trong (1995), The Red River fault system in the Tonkin Gulf, Vietnam, *Tectonophysics*, *243*(3–4), 209–222.
Ru, K., and J. D. Pigott (1986), Episodic rifting and subsidence in the South China Sea, *AAPG Bull.*, *70*, 1136–1155.
Sheriff, R. E. (1980), *Seismic Stratigraphy*, pp. 1–227, Int. Hum. Resour. Dev., Boston, Mass.
Shi, H., and C.-F. Li (2012), Mesozoic and early Cenozoic tectonic convergence-to-rifting transition prior to opening of the South China Sea, *Int. Geol. Rev.*, *54*(15), 1801–1828.
Shipboard Scientific Party (2000). Site 1148, in *Proceedings of Ocean Drilling Program, Initial Reports*, vol. 184, edited by P. Wang et al., pp. 1–103, Ocean Drill. Program, College Station, Tex., doi:10.2973/odp.proc.ir.184.109.2000.
Su, D., N. White, and D. McKenzie (1989), Extension and subsidence of the Pearl River Mouth basin, northern South China Sea, *Basin Res.*, *2*, 205–222.
Taylor, B., and D. E. Hayes (1980), The tectonic evolution of the South China Basin, in *The Tectonic and Geologic Evolution of Southeast Asian Seas and Islands, Part 1*, *Geophys. Monogr. Ser.*, edited by D. E. Hayes, pp. 89–104, AGU, Washington D. C.
Taylor, B., and D. E. Hayes (1983), Origin and history of the South China Sea basin, in *The Tectonic and Geologic Evolution of South Eastern Asian Seas and Islands, II*, *Geophys. Monogr. Ser.*, vol. 27, edited by D. E. Hayes, pp. 23–56, AGU, Washington, D. C.
Teng, L. S. (1990), Geotectonic evolution of the late-Cenozoic arc-continent collision in Taiwan, *Tectonophysics*, *183*, 57–76.
Wang, P., et al. (2000), *Proceedings of Ocean Drilling Program, Initial Report*, vol. 184, Ocean Drill. Program, College Station, Tex.
Wang, P., Q. Li, and C.-F. Li (2014), *Geology of the China Seas*, 687 pp., Elsevier, Oxford, U. K.
Wang, X. J., M. Wu, D. Liang, and A. Yin (1985), Some geochemical characteristics of basalts in the South China Sea [in Chinese], *Geochimia*, *4*, 332–340.
Wessel, P., and W. H. F. Smith (1995), New version of the Generic Mapping Tools (GMT) version 3.0 released, *Eos Trans. AGU*, *76*, 329.

Xu, Y. G., J. X. Wei, H. N. Qiu, H. H. Zhang, and X. L. Huang (2012), Opening and evolution of the South China Sea constrained by studies on volcanic rocks: Preliminary results and a research design, *Chinese Sci. Bull.*, *57*, 3150–3164.

Yan, P., D. Zhou, and Z. Liu (2001), A crustal structure profile across the northern continental margin of the South China Sea, *Tectonophysics*, *338*, 1–21.

Yan, P., H. Deng, H. L. Liu, Z. Zhang, and Y. Jiang (2006), The temporal and spatial distribution of volcanism in the South China Sea region, *J. Asian Earth Sci.*, *27*, 647–659.

Yan, Q. S., X. F. Shi, K. S. Wang, W. Bu, and L. Xiao (2008), Major, trace elements and Sr-Nd-Pb isotope study of Cenozoic alkali basalts of the South China Sea, *Sci. China Ser. D-Earth Sci.*, *51*, 550–566.

Yang, T. F., T. Lee, C.-H. Chen, S.-N. Cheng, U. Knittel, R. S. Punongbayan, and A. R. Rasdas (1996), A double island arc between Taiwan and Luzon: Consequence of ridge subduction, *Tectonophysics*, *258*, 85–101.

Yao, B. (1995), Characteristics and tectonic significance of the Zhongnan-Liyue Fault [in Chinese], *Geol. Res. South China Sea Mem.*, *7*, 1–14.

Yao, B., W. Zeng, Y. Chen, X. Zhang, D. E. Hayes, J. Diebold, P. Buhl, and S. Spangler (1994), *The Geological Memoir of South China Sea Surveyed Jointly by China and USA* [in Chinese], pp. 1–204, China Univ. of Geosci. Press, Wuhan, China.

Yao, Y., H. Liu, C. Yang, B. Han, J. Tian, Z. Yin, J. Gong, and Q. Xu (2012), Characteristics and evolution of Cenozoic sediments in the Liyue Basin, SE South China Sea, *J. Asian Earth Sci.*, *60*, 114–129.

Zhou, X., T. Sun, W. Shen, L. Shu, and Y. Niu (2006), Petrogenesis of Mesozoic granitoids and volcanic rocks in South China: A response to tectonic evolution, *Episodes*, *29*, 26–33.

Zhou, X. M., and W. X. Li (2000), Origin of late Mesozoic igneous rocks in southeastern China: Implications for lithosphere subduction and underplating of mafic magmas, *Tectonophysics*, *326*, 269–287.

Zhu, M., S. Graham, and T. McHargue (2009), The Red River Fault zone in the Yinggehai Basin, South China Sea, *Tectonophysics*, *476*(3), 397–417.